Twisted symmetric trilayer graphene. II. Projected Hartree-Fock study

Fang Xie, Nicolas Regnault, Dumitru Călugăru, B. Andrei Bernevig, and Biao Lian

Phys. Rev. B **104**, 115167 — Published 30 September 2021

DOI: 10.1103/PhysRevB.104.115167

TSTG II: Projected Hartree-Fock Study of Twisted Symmetric Trilayer Graphene

Fang Xie,[1] Nicolas Regnault,[1,2] Dumitru Călugăru,[1] B. Andrei Bernevig,[1,3,4] and Biao Lian[1]

[1]*Department of Physics, Princeton University, Princeton, New Jersey 08544, USA*
[2]*Laboratoire de Physique de l'Ecole normale superieure, ENS, Université PSL, CNRS, Sorbonne Université, Université Paris-Diderot, Sorbonne Paris Cité, 75005 Paris, France*
[3]*Donostia International Physics Center, P. Manuel de Lardizabal 4, 20018 Donostia-San Sebastian, Spain*
[4]*IKERBASQUE, Basque Foundation for Science, Bilbao, Spain*

(Dated: September 13, 2021)

The Hamiltonian of the magic-angle twisted symmetric trilayer graphene (TSTG) can be decomposed into a TBG-like flat band Hamiltonian and a high-velocity Dirac fermion Hamiltonian. We use Hartree-Fock mean field approach to study the projected Coulomb interacting Hamiltonian of TSTG developed in Călugăru *et al.* [Phys. Rev. B **103**, 195411 (2021)] at integer fillings $\nu = -3, -2, -1$ and 0 measured from charge neutrality. We study the phase diagram with w_0/w_1, the ratio of AA and AB interlayer hoppings, and the displacement field, which introduces an interlayer potential U and hybridizes the TBG-like bands with the Dirac bands. At small U, we find the ground states at all fillings ν are in the same phases as the tensor products of a Dirac semimetal with the filling ν TBG insulator ground states, which are spin-valley polarized at $\nu = -3$, and fully (partially) intervalley coherent at $\nu = -2, 0$ ($\nu = -1$) in the flat bands. An exception is $\nu = -3$ with $w_0/w_1 \gtrsim 0.7$, which possibly become a metal with competing orders at small U due to charge transfers between the Dirac and flat bands. At strong U where the bandwidths exceed interactions, all the fillings ν enter a metal phase with small or zero valley polarization and intervalley coherence. Lastly, at intermediate U, semimetal or insulator phases with zero intervalley coherence may arise for $\nu = -2, -1, 0$. Our results provide a simple picture for the electron interactions in TSTG systems, and reveal the connection between the TSTG and TBG ground states.

I. INTRODUCTION

The rich physics discovered in twisted bilayer graphene (TBG), including the correlated insulating phase at integer fillings and the superconducting phase with finite doping have attracted the attention of both experimental and theoretical communities [1–110]. The progress on TBG systems has also inspired interest in other twisted moiré materials. Among the twisted multilayer graphene systems and motivated by theoretical proposals in Refs. [111–120], the twisted symmetric trilayer graphene (TSTG) has recently been realized in experiments [121–123]. Correlated insulating states and superconducting states are also observed in TSTG. Similar to the twisted bilayer graphene, the electron density in TSTG is tunable via gate voltages. Moreover, an external displacement field perpendicular to the graphene sheets can be applied to the system, which makes the band structure also tunable by gate voltages. The experimental discoveries also triggered a deeper theoretical look at this system [124–129].

TSTG is made of three graphene sheets in AAA stacking, with the middle layer twisted by a small angle θ relative to the top and bottom sheets. This lattice structure is shown to be energetically stable [116]. In the absence of the external displacement field, the system has mirror symmetry, by reflection around the graphene middle layer. Therefore we are able to use the eigenstates of this mirror symmetry as the basis: the TSTG decouples into two sectors with $+1$ and -1 mirror eigenvalues, which correspond to a TBG-like Hamiltonian with the effective interlayer hopping enhanced by a $\sqrt{2}$ factor, and a Dirac cone Hamiltonian with a large unrenormalized Fermi velocity, respectively [112]. Similar to the pure TBG system, the TBG-like sector in TSTG exhibits flat bands at the TSTG magic angle $\theta_M \approx 1.5°$, which is $\sqrt{2}$ times of the TBG magic angle. The band dispersion also depends on the parameter $w_0/w_1 \in [0, 1]$, which is the ratio between interlayer in AA and AB hoppings. When an out-of-plane displacement field is turned on, these two mirror sectors will hybridize with each other. Equivalently, the out-of-plane displacement field can be captured by a interlayer potential U. In Ref. [124], we provided the perturbation schemes of the low energy bands in TSTG with and without the displacement field, derived the projected Hamiltonian for TSTG with a screened Coulomb interaction, and carefully analyzed the discrete symmetries and continuous symmetries of the TSTG Hamiltonian. These provide the foundation of the TSTG projected Hamiltonian we study in this paper.

In this paper, we employ the Hartree Fock (HF) mean field theory to study numerically the ground states of the projected interacting Hamiltonian of magic angle TSTG with a screened Coulomb repulsive interaction derived in Ref. [124]. We focus on integer fillings $\nu = -3, -2, -1, 0$, defined as the number of electrons per moiré unit cell relative to the charge neutrality, where insulating or semimetallic behaviors are observed experimentally [121–123]. Our numerical results show that at small U, the TSTG phases at all integer fillings ν are states that can adiabatically connect to the tensor product of a semimetal in the Dirac sector with the TBG sector ground states at flat band fillings ν: the TBG sector flat bands are fully spin-valley polarized at $\nu=-3$, fully intervalley coherent at $\nu=-2$ and 0, and partially intervalley coherent at $\nu=-1$. The only exception is the case of $\nu=-3$ with $w_0/w_1>0.7$, where the TSTG may enter a large Fermi surface metal phase with competing orders, including a potential translation symmetry breaking, due to the charge transfers between the Dirac and TBG sectors. At fillings $\nu=-2,-1,0$, as U increases (at $w_0/w_1>0$), we find a universal first order transition into a phase with zero intervalley coherence, which either remains a semimetal ($\nu=-2,-1$) or may even become an insulator ($\nu=-1,0$). Lastly, at stronger U for which the TSTG free bandwidth exceeds the Coulomb interaction energy scale, all the integer fillings enter a metallic phase with large Fermi surfaces and small or zero valley polarization and intervalley coherence.

The rest of the paper is organized as follows. In Sec. II, we review the single body Hamiltonian of TSTG and its mirror symmetric basis. The projected Hamiltonian into the low energy bands being studied is also discussed. Sec. III presents the Hartree-Fock mean field approximation to the TSTG projected Hamiltonian, the self consistent conditions, and the HF order parameters which characterize the physical properties of the mean field ground state. In Sec. IV, we provide the HF numerical results at integer filling factor $\nu=-3$. The phase diagram and ground state properties are discussed. We have also calculated the HF band structure in different phases. Similarly, the discussion of the HF numerical results at filling factors $\nu=-2,-1$ and 0 are also presented in Secs. V, VI and VII, respectively.

II. INTERACTING MODEL FOR TSTG

We first briefly review the non-interacting Bistritzer-MacDonald Hamiltonian for mirror symmetric twisted trilayer graphene, which can be written as the sum of a TBG Hamiltonian [3] with renormalized interlayer hopping and an independent Dirac fermion Hamiltonian [112, 124]. We also introduce a displacement field perpendicular to the graphene sheets that can couple the Dirac fermion and TBG fermion together. The interacting Hamiltonian projected into the low energy bands is also discussed in this section [124].

A. Single particle Hamiltonian

The twisted trilayer graphene geometry with mirror symmetry was introduced in Refs. [112, 113]. In this article we will use the notations of Ref. [37–39, 70, 86, 87, 100, 124] where the non-interacting model and its symmetries are discussed in detail. We use $\hat{a}^\dagger_{\mathbf{p},\alpha,s,l}$ to represent the electron creation operator with momentum $\mathbf{p}$ measured from the Γ point of single layer graphene Brillouin zone, sublattice $\alpha=A,B$, spin $s=\uparrow,\downarrow$ and layer $l=1,2,3$. Similar to the derivation of Bistritzer-MacDonald model for twisted bilayer graphene, Dirac equation can be used to describe the low energy physics of each individual layer. We define $\mathbf{K}_+=\mathbf{K}_1=\mathbf{K}_3$ as the K point of the bottom and the top layers, and $\mathbf{K}_-=\mathbf{K}_2$ for the middle layer. Here $|\mathbf{K}_\pm|=1.073\text{Å}^{-1}$. For convenience, we also define vectors $\mathbf{q}_j=C_{3z}^{j-1}(\mathbf{K}_+-\mathbf{K}_-)$. The reciprocal lattice of the moiré lattice $\mathcal{Q}_0$ is spanned by the basis vectors $\mathbf{b}_{M1}=\mathbf{q}_3-\mathbf{q}_1$ and $\mathbf{b}_{M2}=\mathbf{q}_3-\mathbf{q}_2$. Adding the vectors $\mathbf{q}_i$ iteratively gives us momentum lattices $\mathcal{Q}_\pm=\mathcal{Q}_0\pm\mathbf{q}_1$, and they form the hexagon lattice in the momentum space. In order to describe the low energy physics, we introduce the electron operators $\hat{a}_{\mathbf{k},\mathbf{Q},\eta,\alpha,s,l}=\hat{a}_{\eta\mathbf{K}_l+\mathbf{k}-\mathbf{Q},\alpha,s,l}$, where $\mathbf{Q}\in\mathcal{Q}_\eta$ if $l=1,3$ or $\mathbf{Q}\in\mathcal{Q}_{-\eta}$ if $l=2$. Without the displacement field along $\hat{z}$ direction, the system is invariant under mirror symmetry m_z which switches the first layer with the third layer, and leaves the middle layer invariant. Therefore, the Bistritzer-MacDonald model for TSTG can be simplified using the following basis transformation:

$$\hat{c}^\dagger_{\mathbf{k},\mathbf{Q},\eta,\alpha,s}=\begin{cases}\frac{1}{\sqrt{2}}\left(\hat{a}^\dagger_{\mathbf{k},\mathbf{Q},\eta,\alpha,s,1}+\hat{a}^\dagger_{\mathbf{k},\mathbf{Q},\eta,\alpha,s,3}\right) & \mathbf{Q}\in\mathcal{Q}_\eta\,,\\ \hat{a}^\dagger_{\mathbf{k},\mathbf{Q},\eta,\alpha,s,2} & \mathbf{Q}\in\mathcal{Q}_{-\eta}\,.\end{cases}\tag{1}$$

where $\mathbf{k}$ belongs to the moiré Brillouin zone (MBZ). These operators (dubbed as *TBG fermions*) have even eigenvalue under m_z transformation. Fermion operators with odd m_z eigenvalue (dubbed as *Dirac fermions*) are given by:

$$\hat{b}^\dagger_{\mathbf{k},\mathbf{Q},\eta,\alpha,s}=\frac{1}{\sqrt{2}}\left(\hat{a}^\dagger_{\mathbf{k},\mathbf{Q},\eta,\alpha,s,1}-\hat{a}^\dagger_{\mathbf{k},\mathbf{Q},\eta,\alpha,3}\right)\quad\mathbf{Q}\in\mathcal{Q}_\eta\,.\tag{2}$$

Since the single body Hamiltonian commutes with m_z transformation in the absence of the external displacement field, it can be written as a block diagonal form:

$$\hat{H}_0=\hat{H}_{\text{TBG}}+\hat{H}_D\,.\tag{3}$$

It can be shown that the Hamiltonian in the mirror symmetric sector $\hat{H}_{\text{TBG}}$ contains $\hat{c},\hat{c}^\dagger$ operators and is identical to the ordinary TBG Hamiltonian [3, 86], with the interlayer hopping parameter multiplied by a factor of $\sqrt{2}$. It reads:

$$\hat{H}_{\text{TBG}}=\sum_{\substack{\mathbf{k}\in\text{MBZ}\\ \mathbf{Q}\mathbf{Q}'\in\mathcal{Q}_\pm\\ \eta,s,\alpha,\eta}}\left[h^{(\eta)}_{\mathbf{Q},\mathbf{Q}'}(\mathbf{k})\right]_{\alpha\beta}\hat{c}^\dagger_{\mathbf{k},\mathbf{Q},\eta,\alpha,s}\hat{c}_{\mathbf{k},\mathbf{Q}',\eta,\beta,s}\,,\tag{4}$$

in which the "first quantized Hamiltonian" of the $\eta=+$ valley is given by:

$$h^{(+)}_{\mathbf{Q},\mathbf{Q}'}(\mathbf{k})=v_F\boldsymbol{\sigma}\cdot(\mathbf{k}-\mathbf{Q})\,\delta_{\mathbf{Q},\mathbf{Q}'}+\sum_{j=1,2,3}\sqrt{2}T_j\delta_{\mathbf{Q}-\mathbf{Q}',\pm\mathbf{q}_j}\tag{5}$$

where $v_F=6104.5\,\text{meV}\cdot\text{Å}$ is the Fermi velocity of single layer graphene, and interlayer hopping matrices T_j are given by:

$$T_j = w_0\sigma_0 + w_1\left[\cos\frac{2\pi(j-1)}{3}\sigma_x + \sin\frac{2\pi(j-1)}{3}\sigma_y\right]. \tag{6}$$

Similar to the TBG Hamiltonian, w_0 and w_1 stand for the interlayer hopping strength around the AA and AB stacking regions, respectively. In this article we use w_0 as a tunable parameter, and keep the value of $w_1 = 110\,\text{meV}$ fixed. Similar to ordinary TBG, we define $w_0 = 0$ as the chiral limit. In the realistic case we have $0 \leq w_0 < w_1$ due to lattice relaxation effects [59, 66, 90, 93]. The $\sqrt{2}$ factor in Eq. (5) comes from the transformation in Eq. (1). Due to the fact that the effective interlayer hopping is stronger, the magic angle of TSTG where the bands around charge neutral point are flat will be around $\theta \approx 1.5°$, which is bigger than the magic angle in TBG [112]. The Hamiltonian in valley $\eta = -$ can be obtained by applying C_{2z} transformation to Eq. (5).

On the other hand, $\hat{H}_D$ only includes the contribution from mirror anti-symmetric sector. It is given by the following expression:

$$\hat{H}_D = \sum_{\substack{\mathbf{k}\in\text{MBZ}\\ \eta,s,\alpha,\beta}}\sum_{\mathbf{Q}\in\mathcal{Q}_\eta}\left[h^{D,\eta}_{\mathbf{Q}}(\mathbf{k})\right]_{\alpha\beta}\hat{b}^\dagger_{\mathbf{k},\mathbf{Q},\eta,\alpha,s}\hat{b}_{\mathbf{k},\mathbf{Q},\eta,\beta,s} \tag{7}$$

in which the first quantized Hamiltonian for Dirac cone reads:

$$h^{D,+}_{\mathbf{Q}}(\mathbf{k}) = v_F\boldsymbol{\sigma}\cdot(\mathbf{k}-\mathbf{Q}), \tag{8}$$

$$h^{D,-}_{\mathbf{Q}}(\mathbf{k}) = \sigma_x h^{D,+}_{-\mathbf{Q}}(-\mathbf{k})\sigma_x. \tag{9}$$

We can introduce an external displacement field perpendicular to the graphene sheets. When this external field is turned on, the mirror symmetry m_z is broken, which will lead to mixing terms between the TBG fermions in the mirror symmetric sector and the Dirac fermions in the mirror anti-symmetric sector. We denote the potential difference between the top and bottom layer by U, and the Hamiltonian which describes the electric field can be written as:

$$\hat{H}_U = \frac{U}{2}\sum_{\mathbf{k},\eta,s\alpha}\sum_{\mathbf{Q}\in\mathcal{Q}_\eta}\sum_{l=1,3}(l-2)\hat{a}^\dagger_{\mathbf{k},\mathbf{Q},\eta,\alpha,s,l}\hat{a}_{\mathbf{k},\mathbf{Q},\eta,\alpha,s,l}. \tag{10}$$

This Hamiltonian can be rewritten using the Dirac and TBG fermions:

$$\hat{H}_U = \frac{U}{2}\sum_{\mathbf{k},\eta,s\alpha}\sum_{\mathbf{Q}\in\mathbf{Q}_\eta}\left(\hat{b}^\dagger_{\mathbf{k},\mathbf{Q},\eta,\alpha,s}\hat{c}_{\mathbf{k},\mathbf{Q},\eta,\alpha,s} + \text{h.c.}\right), \tag{11}$$

which couples the mirror symmetric and anti-symmetric sectors. In conclusion, the non-interacting Hamiltonian can be written as the summation of these three terms:

$$\hat{H}_0 = \hat{H}_{\text{TBG}} + \hat{H}_D + \hat{H}_U. \tag{12}$$

B. Interaction and Projected Hamiltonian

In this article we will assume that the interaction between electrons in TSTG system is given by the Coulomb potential screened by a top and bottom gate. The interaction Fourier transformation reads:

$$V(\mathbf{q}) = \pi\xi^2U_\xi\frac{\tanh(\xi q/2)}{\xi q/2} \tag{13}$$

where $\xi \approx 10\,\text{nm}$ is the distance between the top and bottom gates, and $U_\xi = e^2/\epsilon\xi \approx 24\,\text{meV}$ is the strength of the Coulomb interaction with dielectric constant $\epsilon \sim 6$ [4, 5, 61]. The interacting Hamiltonian can be written as [27, 38, 124]:

$$\hat{H}_I = \frac{1}{2N_M\Omega_c}\sum_{\mathbf{q}\in\text{MBZ}}\sum_{\mathbf{G}\in\mathcal{Q}_0}V(\mathbf{q}+\mathbf{G})\delta\rho_{\mathbf{q}+\mathbf{G}}\delta\rho_{-\mathbf{q}-\mathbf{G}} \tag{14}$$

where Ω_c is the area of moiré unit cell, and N_M is the number of moiré unit cells. $\delta\rho$ is the electron density at momentum $\mathbf{q}+\mathbf{G}$ relative to the charge neutral point and can be written as:

$$\delta\rho_{\mathbf{q}+\mathbf{G}} = \delta\rho^{\hat{c}}_{\mathbf{q}+\mathbf{G}} + \delta\rho^{\hat{b}}_{\mathbf{q}+\mathbf{G}}, \tag{15}$$

$$\delta\rho^{\hat{c}}_{\mathbf{q}+\mathbf{G}} = \sum_{\substack{\mathbf{k},\eta,\alpha,s\\ \mathbf{Q}\in\mathcal{Q}_\pm}}\left(\hat{c}^\dagger_{\mathbf{k}+\mathbf{q},\mathbf{Q}-\mathbf{G},\eta,\alpha,s}\hat{c}_{\mathbf{k},\mathbf{Q},\eta,\alpha,s} - \frac{1}{2}\delta_{\mathbf{q},0}\delta_{\mathbf{G},0}\right), \tag{16}$$

$$\delta\rho^{\hat{b}}_{\mathbf{q}+\mathbf{G}} = \sum_{\substack{\mathbf{k},\eta,\alpha,s\\ \mathbf{Q}\in\mathcal{Q}_\eta}}\left(\hat{b}^\dagger_{\mathbf{k}+\mathbf{q},\mathbf{Q}-\mathbf{G},\eta,\alpha,s}\hat{b}_{\mathbf{k},\mathbf{Q},\eta,\alpha,s} - \frac{1}{2}\delta_{\mathbf{q},0}\delta_{\mathbf{G},0}\right). \tag{17}$$

By projecting the system into the low energy bands, the dimension of Hamiltonian matrix in Hartree Fock calculation will be reduced dramatically, and therefore greatly improving the numerical calculations. By diagonalizing the single particle TBG Hamiltonian $h^{(\eta)}(\mathbf{k})$ and the Dirac Hamiltonian $h^{D,\eta}(\mathbf{k})$, we obtain the dispersion relation $\varepsilon^{\hat{f}}_{m,\eta}(\mathbf{k})$ and the single body wavefunctions $u^{\hat{f}}_{\mathbf{Q}\alpha,m\eta}(\mathbf{k})$ for the TBG and Dirac fermions ($\hat{f} = \hat{c}, \hat{b}$). For each spin and valley, we project the kinetic Hamiltonian into the two bands which are closest to the charge neutral point for both $\hat{H}_{\text{TBG}}$ and $\hat{H}_D$. Therefore, the kinetic part of the projected Hamiltonian can be written in the following form when $U = 0$:

$$H_{\text{TBG}} + H_D = \sum_{\hat{f}=\hat{c},\hat{b}}\sum_{\mathbf{k},m=\pm1,\eta,s}\varepsilon^{\hat{f}}_{m,\eta}(\mathbf{k})\hat{f}^\dagger_{\mathbf{k},m,\eta,s}\hat{f}_{\mathbf{k},m,\eta,s} \tag{18}$$

where the creation operators in band indices are defined as $\hat{f}^\dagger_{\mathbf{k},m,\eta,s} = \sum_{\mathbf{Q}\alpha}u^{\hat{f}}_{\mathbf{Q}\alpha,m\eta}\hat{f}^\dagger_{\mathbf{k},\mathbf{Q},\eta,\alpha,s}$. The Dirac fermions in the antisymmetric sector $\hat{b}$ are degenerate on certain high symmetry lines between the projected bands and the bands above and below when folding over the MBZ, therefore there is an ambiguity of choosing its single-body wavefunction. We provide a careful discussion of this issue and how we solve it in Appendix A.

As shown in Refs. [29, 30, 38, 70], by fixing the sewing matrix of $C_{2z}T$ symmetry to identity (where C_{2z} is the 2-fold rotation about the z axis, and T is the time reversal), one can recombine the TBG flat energy band basis $\hat{c}^\dagger_{\mathbf{k},m,\eta,s}$ into a Chern band basis

$$\hat{d}^\dagger_{\mathbf{k},e_Y,\eta,s} = \frac{\hat{c}^\dagger_{\mathbf{k},+1,\eta,s} + ie_Y \hat{c}^\dagger_{\mathbf{k},-1,\eta,s}}{\sqrt{2}} , \quad (19)$$

where $e_Y = \pm 1$ gives the Chern number of the Chern band basis (which is also the eigenvalue of the Pauli matrix ζ_y in the space of TBG energy band index $m = \pm 1$).

The displacement field term $\hat{H}_U$ in Eq. (11) can also be written using band basis and projected into the lowest bands:

$$H_U = \frac{U}{2} \sum_{\mathbf{k},\eta,s} \sum_{m=\pm1} \sum_{n=\pm1} N^\eta_{mn}(\mathbf{k}) \left(\hat{b}^\dagger_{\mathbf{k},m,\eta,s} \hat{c}_{\mathbf{k},n,\eta,s} + \text{h.c.} \right) , \quad (20)$$

where the displacement field overlap matrices are given by

$$N^\eta_{mn}(\mathbf{k}) = \sum_{\mathbf{Q}\in\mathcal{Q}_\eta,\alpha} u^{\hat{b}*}_{\mathbf{Q}\alpha,m\eta}(\mathbf{k}) u^{\hat{c}}_{\mathbf{Q}\alpha,n\eta} . \quad (21)$$

Thus the projected non-interacting Hamiltonian can be written as the following quadratic form:

$$\begin{aligned} H_0 =& H_{\text{TBG}} + H_D + H_U \\ =& \sum_{\mathbf{k},\hat{f}\hat{f}',\eta\eta',ss'} \mathcal{H}^{(0)}_{\hat{f}m\eta s,\hat{f}'n\eta's'}(\mathbf{k}) \hat{f}^\dagger_{\mathbf{k},m,\eta,s} \hat{f}'_{\mathbf{k},n,\eta',s'} , \end{aligned} \quad (22)$$

in which the matrix $\mathcal{H}^{(0)}(\mathbf{k})$ is given by

$$\begin{aligned} \mathcal{H}^{(0)}_{\hat{f}m\eta s,\hat{f}'n\eta's'}(\mathbf{k}) =& \varepsilon^{\hat{f}}_{m,\eta}(\mathbf{k}) \delta_{\hat{f}\hat{f}'} \delta_{mn} \delta_{\eta\eta'} \delta_{ss'} \\ &+ \frac{U}{2} (N^\eta_{mn}(\mathbf{k}) \delta_{\hat{f}\hat{b}} \delta_{\hat{f}'\hat{c}} + N^{\eta*}_{mn}(\mathbf{k}) \delta_{\hat{f}\hat{c}} \delta_{\hat{f}'\hat{b}}) \delta_{\eta\eta'} \delta_{ss'} . \end{aligned} \quad (23)$$

Here $\varepsilon^{\hat{f}}_{m,\eta}(\mathbf{k})$ is the dispersion of TBG($\hat{f} = \hat{c}$) and Dirac($\hat{f} = \hat{b}$) fermions without displacement field. The eigenvalues of $\mathcal{H}^{(0)}(\mathbf{k})$ can give us the approximate dispersion of the non-interacting TSTG at non-zero displacement field. The projected Hamiltonian can capture the band width of the bands around charge neutrality accurately [124]. We also provide plots comparing the dispersion of the projected Hamiltonian $\mathcal{H}^{(0)}(\mathbf{k})$ and the band structure obtained from the unprojected BM Hamiltonian in Appendix A Fig. S2 [124].

Similarly, the interacting Hamiltonian can also be projected into these bands:

$$H_I = \frac{1}{2N_M\Omega_c} \sum_{\mathbf{q},\mathbf{G}\in\mathcal{Q}_0} V(\mathbf{q}+\mathbf{G}) \overline{\delta\rho}_{\mathbf{q}+\mathbf{G}} \overline{\delta\rho}_{-\mathbf{q}-\mathbf{G}} , \quad (24)$$

in which the density operators after being projected are defined as:

$$\overline{\delta\rho}_{\mathbf{q}+\mathbf{G}} = \sum_{\hat{f}=\hat{c},\hat{b}} \overline{\delta\rho}^{\hat{f}}_{\mathbf{q}+\mathbf{G}} \quad (25)$$

$$\begin{aligned} \overline{\delta\rho}^{\hat{f}}_{\mathbf{q}+\mathbf{G}} =& \sum_{\mathbf{k},m,n,\eta,s} M^{\hat{f},\eta}_{mn}(\mathbf{k},\mathbf{q}+\mathbf{G}) \\ & \left(\hat{f}^\dagger_{\mathbf{k}+\mathbf{q},m,\eta,s} \hat{f}_{\mathbf{k},n,\eta,s} - \frac{1}{2}\delta_{\mathbf{q},0}\delta_{mn} \right) , \end{aligned} \quad (26)$$

$$M^{\hat{f},\eta}_{mn}(\mathbf{k},\mathbf{q}+\mathbf{G}) = \sum_{\mathbf{Q}\alpha} u^{\hat{f}*}_{\mathbf{Q}-\mathbf{G}\alpha,m\eta}(\mathbf{k}+\mathbf{q}) u^{\hat{f}}_{\mathbf{Q}\alpha,n\eta}(\mathbf{k}) . \quad (27)$$

The components of these form factors $M^{\hat{f},\eta}_{mn}(\mathbf{k},\mathbf{q}+\mathbf{G})$ depend on the gauge choice of the single body wavefunctions. As mentioned in Eq. (19), we fix the gauge choice of the single-body wavefunction of the TBG fermions $u^{\hat{c}}_{\mathbf{Q}\alpha,m\eta}(\mathbf{k})$ such that the sewing matrix of $C_{2z}T$ is the identity.

For convenience, we can rewrite the interacting Hamiltonian as the following form:

$$\begin{aligned} H_I =& \frac{1}{2\Omega_{\text{tot}}} \sum_{\mathbf{k},\mathbf{k}',\mathbf{q}} \sum_{\eta\eta'ss'} \sum_{\hat{f},\hat{f}'=\hat{c},\hat{b}} \sum_{mnm'n'} \tilde{V}^{(\hat{f}\eta;\hat{f}'\eta')}_{mn;m'n'}(\mathbf{q};\mathbf{k},\mathbf{k}') \\ &\times \left(\hat{f}^\dagger_{\mathbf{k}+\mathbf{q},m,\eta,s} \hat{f}_{\mathbf{k},n,\eta,s} - \frac{1}{2}\delta_{\mathbf{q},0}\delta_{mn} \right) \\ &\times \left(\hat{f}'^\dagger_{\mathbf{k}'-\mathbf{q},m',\eta',s'} \hat{f}'_{\mathbf{k}',n',\eta',s'} - \frac{1}{2}\delta_{\mathbf{q},0}\delta_{m'n'} \right) , \end{aligned} \quad (28)$$

in which the matrix elements $\tilde{V}^{(\hat{f}\eta;\hat{h}\eta')}_{mn;m'n'}(\mathbf{q};\mathbf{k},\mathbf{k}')$ are given by:

$$\begin{aligned} &\tilde{V}^{(\hat{f}\eta;\hat{h}\eta')}_{mn;m'n'}(\mathbf{q};\mathbf{k},\mathbf{k}') \\ =& \sum_{\mathbf{G}} V(\mathbf{q}+\mathbf{G}) M^{\hat{f},\eta}_{mn}(\mathbf{k},\mathbf{q}+\mathbf{G}) M^{\hat{h},\eta'}_{m'n'}(\mathbf{k}',-\mathbf{q}-\mathbf{G}) . \end{aligned} \quad (29)$$

The mean field Hamiltonian will have a simpler form using this notation, as we will discuss in Sec. III.

In this paper, we fix the twist angle to $\theta = 1.51^\circ$, which is near the magic angle of TSTG and gives rise to flat bands in the mirror symmetric sector. Since both the band structure and the wavefunctions of the mirror symmetric sector depend on the parameter w_0, the projected Hamiltonian also depends on w_0. And by adding all the terms in kinetic energy and potential energy, we obtain the tunable Hamiltonian with parameters w_0 and U:

$$H(w_0,U) = H_{\text{TBG}}(w_0) + H_D + H_U(w_0,U) + H_I(w_0) . \quad (30)$$

Similar to that in TBG, we define $w_0 = 0$ as the chiral limit, and $H_{\text{TBG}}(w_0) = 0$ (zero TBG bandwidth) as the flat (TBG band) limit. In these limits or their combinations, the symmetry of the TSTG is enhanced to a $U(4)$ symmetry in the combined spin and valley space [124]. In this paper, we will not tune the bandwidth in the mirror symmetric (TBG) sector, therefore the non-interacting band structure will only depend on w_0 and U (at the fixed twist angle $\theta = 1.51°$ and AB/BA interlayer hopping strength $w_1 = 110\,\text{meV}$).

III. HARTREE-FOCK THEORY

We perform Hartree Fock (HF) mean field calculations for the projected Hamiltonian we obtained in Eq. (30), which is at fixed twist angle $\theta = 1.51°$. In Appendix B, we provide a more detailed discussion of the HF calculations. In this section, we focus on the assumption and the quantities that we will rely on in the rest of our paper.

In Refs. [29, 61, 70, 100, 107], it has been shown that the ground states of TBG at integer fillings (integer number of electrons per moiré unit cell, relative to the charge neutral point) around the chiral flat band limit (i.e. the value of w_0/w_1 is small and disregarding the flat band dispersion) are correlated insulator states (sometimes with non-zero Chern number) without translation symmetry breaking. This picture is expected to be valid till reasonably large physical w_0/w_1 values (depending on electron fillings) [62, 85, 100]. Meanwhile, the high Fermi velocity and vanishing Fermi surfaces of the Dirac fermions make them unlikely to contribute to translation symmetry breaking (which requires certain low energy Fermi surface nestings).

Therefore, we assume there is no translation symmetry breaking in our HF calculation for TSTG (with a notable exception in Appendix C 1 where we discuss the possible CDW order at M_M point at $\nu = -3$ filling). This assumption simplifies our numerical calculation by reducing the number of HF mean field order parameters. For this reason, within the assumption, the HF mean field order parameter can be defined as the following 16×16 matrix at each $\mathbf{k}$:

$$\Delta_{\hat{f}m\eta s;\hat{f}'n\eta' s'}(\mathbf{k}) = \left\langle \hat{f}^\dagger_{\mathbf{k},m,\eta,s} \hat{f}'_{\mathbf{k},n,\eta',s'} - \frac{1}{2}\delta_{\hat{f}\hat{f}'}\delta_{mn}\delta_{\eta\eta'}\delta_{ss'} \right\rangle, \tag{31}$$

where $\hat{f}, \hat{f}'$ stand for the TBG and Dirac fermion operators. The matrix $\Delta(\mathbf{k})$ is the single-body density matrix at each momentum $\mathbf{k}$. As we explained, this assumption of no translation breaking is reasonable when w_0/w_1 is small (typically $w_0/w_1 \lesssim 0.7$), and it is possible that our assumption will be violated for large w_0/w_1 [61, 100]. Therefore, the Hartree Fock result is less trustable when w_0/w_1 gets bigger.

For an arbitrary momentum $\mathbf{k}$, the Hartree and Fock mean field Hamiltonians are given by the following:

$$\mathcal{H}^{(H)}_{\hat{f}m\eta s,\hat{f}'n\eta' s'}(\mathbf{k}) = \frac{1}{\Omega_{\text{tot}}} \sum_{\mathbf{k}',\hat{f}',m'n',\eta'',s''} \tilde{V}^{(\hat{f}\eta;\hat{f}'\eta'')}_{mn;m'n'}(0;\mathbf{k},\mathbf{k}') \times \Delta_{\hat{f}'m'\eta''s'';\hat{f}'n'\eta''s''}(\mathbf{k}')\delta_{\eta\eta'}\delta_{ss'} \tag{32}$$

$$\mathcal{H}^{(F)}_{\hat{f}m\eta s,\hat{f}'n\eta' s'}(\mathbf{k}) = -\frac{1}{\Omega_{\text{tot}}} \sum_{\mathbf{k}',m'n'} \tilde{V}^{(\hat{f}'\eta';\hat{f}\eta)}_{m'n;mn'}(\mathbf{k}'-\mathbf{k};\mathbf{k},\mathbf{k}') \times \Delta_{\hat{f}'m'\eta' s';\hat{f}n'\eta s}(\mathbf{k}') \tag{33}$$

Together with the non-interacting term $\mathcal{H}^{(0)}(\mathbf{k})$ defined in Eqs. (22) and (23), we obtain the Hartree Fock Hamiltonian $\mathcal{H}^{HF}(\mathbf{k}) = \mathcal{H}^{(0)}(\mathbf{k}) + \mathcal{H}^{(H)}(\mathbf{k}) + \mathcal{H}^{(F)}(\mathbf{k})$. By diagonalizing the Hartree Fock Hamiltonian, we obtain the HF band structure $E_i(\mathbf{k})$, which is related to the dispersion of the charge excitations, and the corresponding wavefunction $\phi_{\hat{f}m\eta s,i}(\mathbf{k})$:

$$\sum_{\hat{f}',n,\eta',s'} \mathcal{H}^{HF}_{\hat{f}m\eta s,\hat{f}'n\eta' s'}(\mathbf{k})\phi_{\hat{f}'n\eta' s',i}(\mathbf{k}) = E_i(\mathbf{k})\phi_{\hat{f}m\eta s,i}(\mathbf{k}) \tag{34}$$

For a filling factor ν, which is defined as the number of electrons per moiré unit cell relative to charge neutrality, the HF ground state is given by occupying the single particle states $E_i(\mathbf{k})$ (where $i = 1, \cdots, 16$ at each $\mathbf{k}$) from low to high up to filling ν. For each single body state $E_i(\mathbf{k})$, valley polarization $v_i(\mathbf{k})$ can be defined as:

$$v_i(\mathbf{k}) = \sum_{\hat{f}ms\eta\eta'} \phi^*_{\hat{f}m\eta s,i}(\mathbf{k})(\tau_z)_{\eta\eta'}\phi_{\hat{f}m\eta' s,i}(\mathbf{k}), \tag{35}$$

and the valley physics of the system can be captured by $v_i(\mathbf{k})$ of each individual occupied state at every $\mathbf{k}$.

The self-consistent condition also gives a relation between these wavefunctions and the order parameter:

$$\Delta_{\hat{f}m\eta s;\hat{f}'n\eta' s'}(\mathbf{k}) = \sum_{i\in\text{occupied}} \Big(\phi^*_{\hat{f}m\eta s,i}(\mathbf{k})\phi_{\hat{f}'n\eta' s',i}(\mathbf{k}) - \frac{1}{2}\delta_{\hat{f}\hat{f}'}\delta_{mn}\delta_{\eta\eta'}\delta_{ss'} \Big). \tag{36}$$

For each integer filling factor ν, we use various initial conditions in our HF calculation, and we choose the result with the lowest energy. Detailed discussion about the choices of initial conditions at different filling factors can be found in Appendix B. In this article, the filling factor ν is measured from the charge neutrality, and it is related with the order parameter in Eq. (36) by:

$$\nu = \frac{1}{N_M} \sum_{\mathbf{k},\hat{f},m,\eta,s} \Delta_{\hat{f}m\eta s;\hat{f}m\eta s}(\mathbf{k}). \tag{37}$$

Moreover, since the particle numbers of Dirac fermion and TBG fermion are conserved when the displacement field is turned off, we can define the filling factors (measured from the charge neutrality) for these fermion flavors separately:

$$\nu_{\rm TBG} = \frac{1}{N_M} \sum_{\mathbf{k},m,\eta,s} \Delta_{\hat{c}m\eta s;\hat{c}m\eta s}(\mathbf{k}) \,, \tag{38}$$

$$\nu_D = \frac{1}{N_M} \sum_{\mathbf{k},m,\eta,s} \Delta_{\hat{b}m\eta s;\hat{b}m\eta s}(\mathbf{k}) \,. \tag{39}$$

The summation of these two quantities is the total filling factor:

$$\nu = \nu_D + \nu_{\rm TBG} \,. \tag{40}$$

For the projected bands we keep, the two filling factors range within $\nu_D \in [-4, 4]$ and $\nu_{\rm TBG} \in [-4, 4]$, respectively. We will be focusing on total integer fillings $\nu = -3, -2, -1, 0$ in this paper. Since the physics at filling $-\nu$ is particle-hole symmetric to that at filling ν [124], it is sufficient to study fillings $\nu \leq 0$.

Various physical quantities can be derived from $\Delta_{\hat{f}m\eta s;\hat{f}'n\eta' s'}(\mathbf{k})$, which can be used to describe the nature of the ground state, such as the intervalley coherence and valley polarization. As shown in Ref. [70], the ground state at $\nu = \pm 2$ filling in TBG has intervalley coherence when the system is non-chiral non-flat. In order to measure the coherence between the two valleys, we define the quantity $\mathcal{C}$ which is based on the norm of the off-diagonal block in valley space:

$$\mathcal{C} = \frac{1}{N_M} \sum_{\mathbf{k}\in \mathrm{MBZ}} \sum_{\hat{f}\hat{f}',mn,ss'} |\Delta_{\hat{f}m+s;\hat{f}'n-s'}(\mathbf{k})|^2 \,, \tag{41}$$

where N_M is the number of moiré lattice sites. This quantity includes both the contribution from the TBG flat bands and the Dirac fermions. Its value is

$$\mathcal{C} = \frac{n}{4} \tag{42}$$

if there are n filled TBG flat bands which are fully intervalley coherent.

The expectation value of any single-body quantity can be obtained from the Hartree-Fock order parameter $\Delta(\mathbf{k})$. In this article, we calculate three quantities that we will now define: the valley polarization N_v, the spins in each valley S^η and the quantity Ch which provides information about the Chern number of the occupied TBG fermions.

The valley polarization N_v is the electron number difference between the two valleys. This can also be obtained from the order parameter:

$$N_v = \sum_{\mathbf{k}} \sum_{\hat{f}=\hat{c},\hat{b}} \sum_{\eta\eta' ms} (\tau_z)_{\eta\eta'} \Delta_{\hat{f}m\eta s;\hat{f}m\eta' s}(\mathbf{k}) \,, \tag{43}$$

where τ_z is the Pauli z matrix in valley space.

Similarly, we can track the spin order. Due to the U(2)×U(2) symmetry of the system, the total spin of the two valleys are conserved independently. For each valley η, the semi-classical total spin per moiré unit cell $\vec{S}^\eta$ can be obtained by the following equation:

$$2\vec{S}^\eta(\mathbf{k}) = \frac{1}{N_M} \sum_{\mathbf{k}} \sum_{\hat{f}=\hat{c},\hat{b}} \sum_{mss'} (\vec{s})_{ss'} \Delta_{\hat{f}m\eta s;\hat{f}m\eta s'}(\mathbf{k}) \,, \tag{44}$$

where $\vec{s} = (s_x, s_y, s_z)$ are the Pauli matrices in spin space.

Finally, we can define a quantity within the TBG band sector:

$$\mathrm{Ch} = \frac{1}{N_M} \sum_{\mathbf{k}} \sum_{\eta smn} (\zeta_y)_{mn} \Delta_{\hat{c}m\eta s;\hat{c}n\eta s}(\mathbf{k}) \,, \tag{45}$$

where ζ_y is the Pauli y matrix in the space of the energy band index m. If the Dirac bands and the TBG bands in the HF Hamiltonian are decoupled (e.g. at $U = 0$ and without m_z breaking order parameters), Ch characterizes the Chern number in the TBG sector when the TBG sector is insulating, which can be seen by transforming Ch into the Chern band basis in Eq. (19). Generically (e.g., $U > 0$), Ch is not necessarily an integer, but it is related with the Chern number of the (partially or fully) occupied TBG flat band basis. For example, this value is close to ± 2 if the two occupied TBG flat bands have the same Chern number. Similar to the filling factor for Dirac and TBG fermion flavors, this quantity is a useful characterization of the many-body state when U is close to zero.

We perform the HF calculations on a C_{3z} preserving $N_L \times N_L$ momentum lattice in the MBZ (see Fig. S1 in the supplementary material), with N_L up to 10. As discussed in Appendix B, we are also able to obtain the band structure plot along high symmetry lines by using the HF order parameters we obtained on these $N_L \times N_L$ lattices. In the band structure plots, we use subscript M to denote the high symmetry points in the moiré Brillouin zone. Our HF calculations are restricted within the pamameter ranges $0.1 \leq w_0/w_1 \leq 1$ and $U \geq 0$. We do not discuss the HF calculation in the chiral limit $w_0 = 0$ in this paper, the convergence of which is difficult due to the enhanced symmetry and enlarged ground state degeneracy manifold. We note that the realistic TSTG is always away from the $w_0 = 0$ chiral limit.

IV. NUMERICAL RESULTS AT FILLING FACTOR $\nu = -3$

We start our discussion about HF calculations for TSTG with filling factor $\nu = -3$. As a comparison, the ground state at $\nu = -3$ filling in TBG at small w_0 and small nonzero bandwidth is a spin and valley polarized Chern insulator state with Chern number ± 1, and may enter translation or rotation symmetry breaking phases at large w_0, which has been predicted in Refs. [29, 70, 100, 107]. In this section, we will explore the HF ground states in TSTG at $\nu = -3$ in the param-

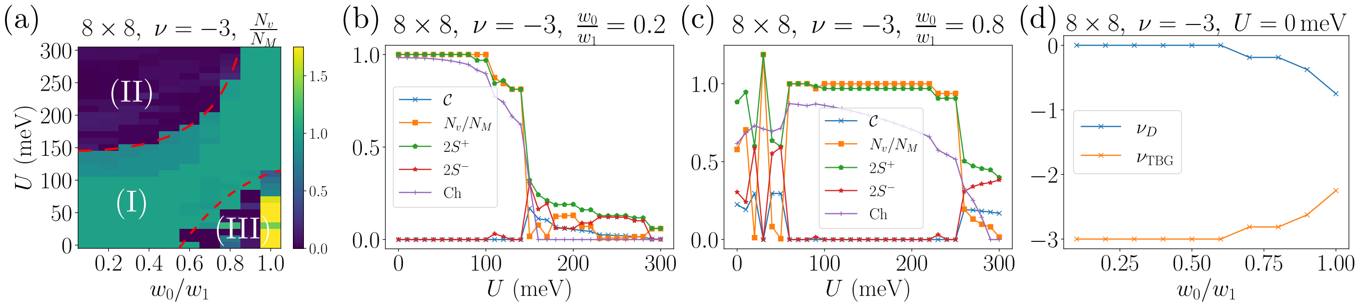

FIG. 1. (a) The phase diagram at filling factor $\nu = -3$ obtained on 8×8 momentum lattice in the (w_0, U) plane. The color represents the valley polarization N_v/N_M of the ground state. (b) The displacement field dependence of other quantities $\mathcal{C}, N_v, S^{\pm}$ and Ch on 8×8 lattice at $w_0/w_1 = 0.2$. (c) Similar to sub-figure (b), the displacement field dependence of these quantities with $w_0/w_1 = 0.8$. (d) The filling factors for Dirac fermions and TBG fermions as a function of w_0. In this plot, the interlayer potential is fixed to be $U = 0\,$meV.

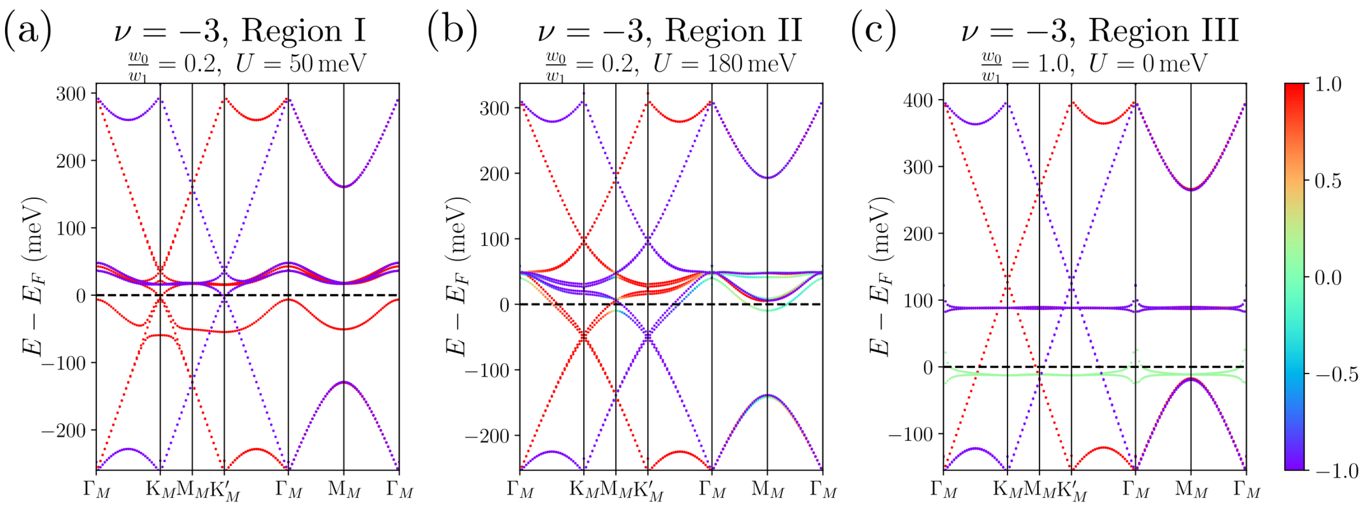

FIG. 2. Some typical HF band structures illustrating the three regions of the phase diagram at filling factor $\nu = -3$ on 10×10 momentum lattice. (a) The band structure in region I with $w_0/w_1 = 0.2$ and $U = 50\,$meV. (b) The band structure in region II with $w_0/w_1 = 0.2$ and $U = 180\,$meV. (c) The band structure in region III with $w_0/w_1 = 1$ and $U = 0\,$meV. The color of each point represents the valley polarization $v_i(\mathbf{k})$ of each single body state, which is defined in Eq. (35).

eter space of w_0/w_1 and U (see Eq. (30) for definition).

Here we restrict the parameter ranges within $0.1 \le w_0/w_1 \le 1$ and $0 \le U \le 300\,$meV. The maximal value of U is motivated by the experimental results [122]. The valley polarization N_v as a function of w_0 and U is shown in Fig. 1(a). We find the HF ground states show different behaviors in three different parameter regions, which are labeled by I, II and III in Fig. 1(a). We also calculate other physical quantities, including $\mathcal{C}, N_v, S^{\pm}$ and Ch, the values of which along certain line cuts in the parameter space are shown in Fig. 1(b) and (c). Based on these quantities, we describe the TSTG phases in the three regions in details below.

Region I: we find $\mathcal{C} \approx 0, N_v/N_M \approx 1, 2S^+ \approx 1, 2S^- \approx 0$ and Ch ≈ 1 throughout the whole region (Fig. 1(b) and (c)). This indicates that the ground state is a spin-valley polarized state dominantly occupying one Chern band in the TBG sector (defined in Eq. (19)) of a particular spin and valley. In particular, at $U = 0$, where the electron numbers in the Dirac sector and the TBG sector are both conserved, we find $\nu_D = 0$ and $\nu_{\rm TBG} = -3$ within region I (see $w_0/w_1 < 0.6$ in Fig. 1(d)). Therefore, in region I, the $\nu = -3$ HF ground state at $U = 0$ is the tensor product of the $\nu_{\rm TBG} = -3$ TBG spin-valley polarized Chern insulator and the Dirac fermion semimetal at charge neutrality $\nu_D = 0$. The ground states at $U > 0$ in region I are adiabatically in the same semimetal phase. As an example, the band structure at $w_0/w_1 = 0.2$ and $U = 50\,$meV is shown in Fig. 2(a), which is almost a Dirac semimetal. At $U > 0$, where the Dirac and TBG sectors are hybridized, the gapless Dirac nodes are due to the $C_{2z}T$ symmetry within the empty valley-spin flavors, as shown in Appendix D. The color (from red to purple) indicates the valley polarization of of each band, and an occupied flat band can be seen clearly.

Region II: we find the valley polarization N_v/N_M drops abruptly to small values near zero, and so do the other quantities as shown in Fig. 1(b) in this region where the displacement field is large. Accordingly, the HF ground state can be understood as a metal with little spin/valley polarization or intervalley coherence. A typical HF band structure in region II is shown in Fig. 2(b), which has a large Fermi surface around K_M (K'_M) point in valley $\eta = +$ ($\eta = -$), showing that the system is a metal. A sharp phase boundary between region I and II can be identified in Fig. 1(a), which is at $U \approx 150\,\mathrm{meV}$ when $w_0/w_1 = 0.2$, and at $U \approx 250\,\mathrm{meV}$ when $w_0/w_1 = 0.8$. The reason for such a metallic phase is that a large U significantly hybridizes the Dirac sector and the TBG sector, and turns the flat bands near K_M (K'_M) point of valley $+$ ($-$) into dispersive Dirac fermions with kinetic energies comparable to the interaction energies. This leads to a Fermi surface reconstruction, where electrons prefer to occupy the electron states near the K_M and K'_M points with lower kinetic energies and form a metal. We provide the non-interacting band width as a function of w_0/w_1 and U in Figs. S4(a) and (b) of Appendix A. The phase boundary between region I and II is close to an equal value contour in these figures, which also implies that the transition to the metallic phase happens as the non-interacting bandwidth exceeds a critical value around the order of the interaction energy scale.

Region III: we find that the HF ground state exhibit competing orders in this region which is located in the weak displacement field region with $w_0/w_1 \gtrsim 0.6$. In Fig. 1(c) we plot the HF mean field quantities, e.g. $\mathcal{C}$, $S^{\pm}$ and Ch, at $w_0/w_1 = 0.8$ with respect to U. When $U < 50\,\mathrm{meV}$ (region III), we see all the quantities are strongly oscillating. Moreover, we also notice strong size effect in this region, which can be seen by considering other system sizes at $w_0/w_1 = 0.8$, as discussed in Appendix C. In previous numerical studies in TBG systems [62, 85, 100] (which do not have the U parameter), it has been shown that the translation symmetry of the TBG at filling $\nu = -3$ could be broken at large w_0/w_1 (typically $w_0/w_1 \gtrsim 0.7$). Therefore, we expect the ground states in region III not to be accurately captured by our HF calculation, which does not allow translation symmetry breaking. In Appendix C 1, we provide numerical evidence for a translation symmetry breaking phase via a modified HF calculation. Nevertheless, we provide some universal observation of our HF results in region III. In Fig. 1(d), we plot ν_D and $\nu_{\mathrm{TBG}} = -3 - \nu_D$ as a function of w_0/w_1 at $U = 0$. We find the Dirac electron filling ν_D is 0 for $w_0/w_1 < 0.6$ (i.e., in region I), but begins to decrease as w_0/w_1 increases beyond 0.6 (i.e., in region III). This indicates that electrons are transferred from the Dirac valence bands into the TBG flat bands in region III, making $\nu_D < 0$ and $\nu_{\mathrm{TBG}} > -3$. For instance, when $w_0 = w_1$ at $U = 0$, our HF calculation shows that $\nu_D \approx -1$ and $\nu_{\mathrm{TBG}} \approx -2$, the HF band structure of which is shown in Fig. 2(c). The Fermi level of this HF band structure in region III is far from the Dirac point energy, giving rise to a metal with large Fermi surfaces. Therefore, the ground states in region III are likely to be metals with competing orders, such as translation symmetry breaking.

In summary, at $\nu = -3$, we have identified three phases in three regions of Fig. 1(a). In region I the ground state is almost a spin-valley polarized semimetal, in region II the ground state is a metal with little spin/valley polarization or intervalley coherence, while in region III the ground state may be a metal with competing orders.

V. NUMERICAL RESULTS AT FILLING FACTOR $\nu = -2$

In this section, we study the HF results for TSTG at integer filling $\nu = -2$. By comparison, in TBG systems, the ground state at $\nu = -2$ at small w_0 and small bandwidth is given by an intervalley coherent insulator with Chern number 0, which has been predicted in Refs. [29, 61, 70, 100, 107]. At large w_0, the TBG ground state may become a metal [39]. However, there is no evidence of translation symmetry breaking at $\nu = -2$ in TBG so far. Therefore, we also conjecture that translation breaking is less likely in the TSTG at $\nu = -2$, and thus regard our HF results as more reliable than at $\nu = -3$ in the large w_0/w_1 region.

Our HF results for TSTG at $\nu = -2$ identified 3 distinct regions I, II, III in the w_0/w_1 and U parameter space as shown in Fig. 3(a). In Fig. 3(a), the color scale indicates the $\nu = -2$ ground state intervalley coherence $\mathcal{C}$, defined in Eq. (41) (note that this is different from the $\nu = -3$ phase diagram Fig. 1(a), where valley polarization is shown by color, while intervalley coherence is near zero). Other HF quantities along certain constant w_0/w_1 line cuts are shown in Fig. 3(b) and (c). From these quantities, we can see clear phase transitions between regions I and II, and between regions II and III. We now describe the HF ground states in the three regions, respectively.

Region I: this region contains the entire range of w_0/w_1 up to some w_0-dependent U value. There we find $\mathcal{C} \approx 0.5$, Ch ≈ 0, $N_v/N_M \approx 0$ and $2S^{\pm} \approx 1$. This implies that there are two fully intervalley coherent flat bands occupied, which have the same spin and have zero total Chern number. This is the same as the TBG ground state at $\nu = -2$ filling. When $U = 0$ in region I, the electron numbers in the Dirac sector and the TBG sector are conserved, respectively, and the HF ground state is almost the tensor product of the $\nu_{\mathrm{TBG}} = -2$ intervalley coherent TBG ground state predicted in Refs. [29, 61, 70, 100, 107] and the Dirac band ground state at charge neutrality $\nu_D = 0$. A typical band structure in region I at $w_0/w_1 = 0.8$ and $U = 0$ is given in Fig. 4(a), where the valley polarization values $v_i(\mathbf{k})$ of the occupied single body states (defined in Eq. (35)) are represented by color. One can see the valley polarization of the 2 occupied flat bands are approximately zero, consistent with an intervalley coherent state. The $\nu = -2$ ground state in region I is thus almost an intervalley coherent semimetal,

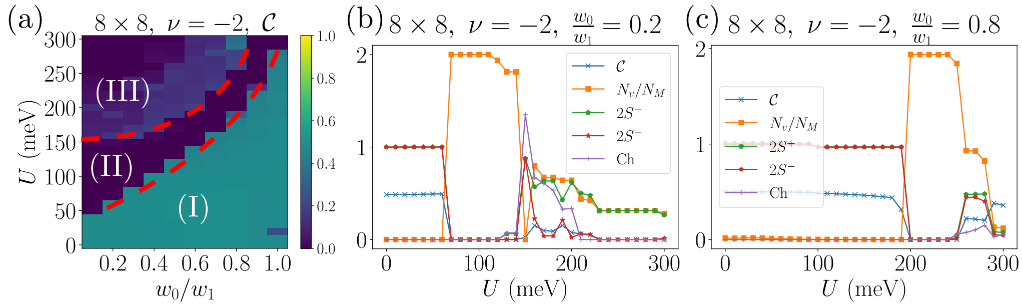

FIG. 3. (a) The phase diagram at filling factor $\nu = -2$ obtained on a 8×8 momentum lattice in the (w_0, U) plane, and the color represents the intervalley coherence, which is defined in Eq. (41). (b) and (c) The displacement field dependence of physical quantities $\mathcal{C}, N_v, \mathrm{Ch}$ and $S^{\pm}$ on a 8×8 at fixed $w_0/w_1 = 0.2$ (b) and $w_0/w_1 = 0.8$ (c). By considering the different HF parameters and band structure, we can define three different regions in the phase diagram, denoted I, II and III in (a).

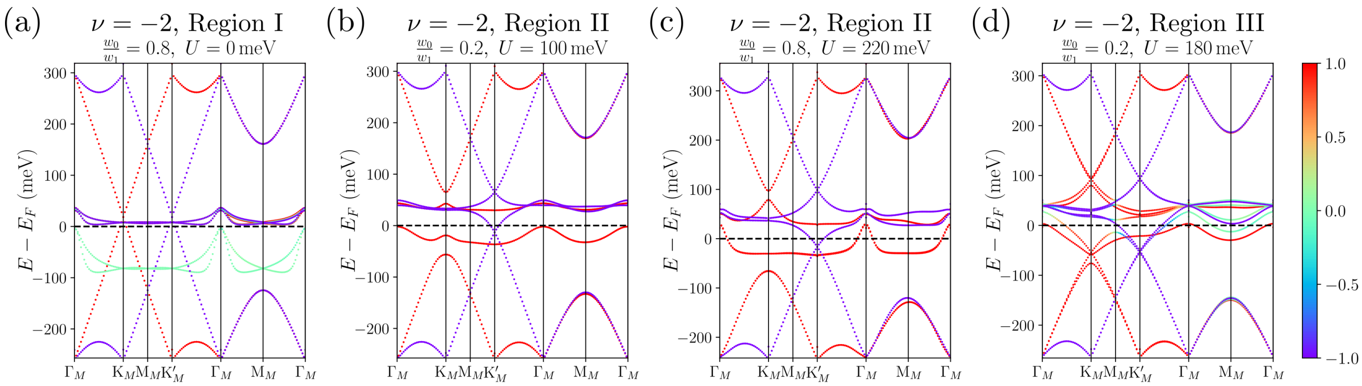

FIG. 4. The HF band structure at $w_0/w_1 = 0.8$ for $U = 0$ (a), at $w_0/w_1 = 0.2$ for $U = 100\,\mathrm{meV}$ (b), at $w_0/w_1 = 0.8$ for $U = 220\,\mathrm{meV}$ (c) and at $w_0/w_1 = 0.2$ for $U = 180\,\mathrm{meV}$ (d) on a 10×10 lattice at filling factor $\nu = -2$. The color represents the valley polarization $v_i(\mathbf{k})$ of each single body state defined in Eq. (35).

in which the Dirac fermion is slightly doped away from the Dirac nodes. In particular, at $U > 0$ where the Dirac and TBG sectors are hybridized, the gapless Dirac nodes are protected by a remaining anti-unitary symmetry $\mathcal{G}_\gamma$ ($\mathcal{G}_\gamma^2 = 1$), which is a combination of the $C_{2z}T$ and a relative intervalley phase rotation (see Appendix D).

Region II: the interlayer potential U is intermediate, and we find $\mathcal{C} \approx 0, N_v/N_M \approx 2, \mathrm{Ch} \approx 0$ and $2S^{\pm} \approx 0$. This indicates that the ground state becomes a valley polarized state, and the two occupied TBG flat bands approximately have zero total Chern number. We plot two typical HF band structures with different w_0/w_1 values in Fig. 4(b) and (c). In both of the band structure plots, the valley polarization values of occupied single body states in the flat bands are $v_i(\mathbf{k}) \approx 1$. The occupied flat bands with smaller (larger) w_0/w_1 value has smaller (larger) band width. The band structures plots also show that there is a small electron pocket around K'_M point, and a small hole pocket around Γ_M point, indicating the system is almost a semimetal with a small Fermi surface.

Region III: the interlayer potential U is further increased (e.g., $U \gtrsim 150\,\mathrm{meV}$ at $w_0/w_1 = 0.2$, and $U \gtrsim 280\,\mathrm{meV}$ at $w_0/w_1 = 0.8$), the valley polarization N_v/N_M drops significantly, and the intervalley coherence slightly re-enters, as shown in Fig. 3(b) and (c). In this case, the $\nu = -2$ TSTG enters a metallic phase with large Fermi surfaces. A HF band structure in this region is shown in Fig. 4(c). Similar to the region II phase at filling $\nu = -3$, the region III phase at $\nu = -2$ here is due to the change of flat bands into high energy dispersive Dirac bands near K_M (K'_M) point of valley $+$ $(-)$ at large U, yielding transitions into less valley polarized metal with large Fermi surfaces.

To summarize, the phase diagram at filling factor $\nu = -2$ can be roughly separated into three regions, as shown in Fig. 3(a). In the small U region I, the ground state is nearly an intervalley coherent semimetal and is adiabatically connected with the tensor product of the TBG ground state and a high velocity Dirac fermion at charge neutrality. In region II with intermediate U, the ground state is fully valley polarized and almost a semimetal. Finally, in region III with large U, the system enters a metal phase with partial valley polarization.

VI. NUMERICAL RESULTS AT FILLING FACTOR $\nu = -1$

In this section, we discuss the HF calculation results for TSTG at filling factor $\nu = -1$. We first recall that the ground state at $\nu = -1$ in nonchiral-nonflat TBG systems carries a Chern number $\nu_C = \pm 1$ and has two intervalley coherent bands and one valley polarized band occupied, as shown in Refs. [70, 107]. Similar to filling $\nu = -3$ and -2, we expect the $\nu = -1$ TSTG ground state at small w_0/w_1 and $U = 0$ to be the tensor product of the TBG ground state at this filling and the half filled Dirac fermion bands.

The intervalley coherence $\mathcal{C}$ of the TSTG HF ground state at $\nu = -1$ as a function of U and w_0/w_1 is represented by the color code in Fig. 5(a). Other HF quantities at $w_0/w_1 = 0.2$ and $w_0/w_1 = 0.8$ are shown in Figs. 5(b) and (c), respectively. Based on these quantities and the HF band structures, we are able to identify four different regions I, II, III and IV in w_0/w_1 and U parameter space as shown in Fig. 5(a). We now describe the HF mean field results in these regions.

Region I: this region encompasses the entire range of w_0/w_1, and up to certain w_0/w_1-dependent U value, and we find that $\mathcal{C} \approx 0.5$, Ch ≈ 1, $N_v/N_M \approx 1$, $2S^+ \approx 1$ and $2S^- \approx 0$. The value of intervalley coherence indicates that among the three occupied TBG flat bands, two of them are intervalley coherent. These values also imply that the HF ground state at $U = 0$ is approximately equal to the tensor product of a $\nu_{\text{TBG}} = -1$ intervalley coherent state [70, 107] and a half-filled Dirac semimetal. Fig. 6(a) shows a typical HF band structure in region I at $w_0/w_1 = 0.8$ and $U = 0$. Among the three occupied flat bands in Fig. 6(a), two of them have zero valley polarization, while the other one is valley polarized, which agrees with the expected ground state in the TBG sector. The $U > 0$ ground states of region I is adiabatically connected to the $U = 0$ ground state. Therefore, region I is a semimetal phase with partially intervalley coherent flat bands. Similar to the $\nu = -3$ case, the gapless Dirac nodes at $U > 0$ are protected by the $C_{2z}T$ symmetry within an empty valley-spin flavor, as shown in Appendix D.

Region II: the displacement field is intermediate in this region (e.g. $80\,\text{meV} \lesssim U \lesssim 150\,\text{meV}$ at $w_0/w_1 = 0.2$, or $220\,\text{meV} \lesssim U \lesssim 280\,\text{meV}$ at $w_0/w_1 = 0.8$). We find that the values of HF quantities N_v/N_M, Ch and $S^\pm$ are close to their values in region I. However, the intervalley coherence $\mathcal{C}$ vanishes abruptly in this region. We present a HF band structure at $w_0/w_1 = 0.8$ and $U = 240\,\text{meV}$ in Fig. 6(b). The valley polarization of the three occupied flat bands are $v_i(\mathbf{k}) \approx \pm 1$. The band structure also shows small electron pocket around K'_M point, and hole pocket around Γ_M point, which means the system is also almost a semimetal without intervalley coherence.

Region III: the displacement field in this region (which is $160\,\text{meV} \lesssim U \lesssim 220\,\text{meV}$ at $w_0/w_1 = 0.2$) is stronger than that in the region II. We find the valley polarization N_v/N_M drops to zero, and the intervalley coherence slightly increases to $\mathcal{C} \approx 0.2$, as shown in Fig. 5(b). The HF band structure in this region, which can be found in Fig. 6(c), shows that there is a direct band gap around the Fermi level. Therefore, we identify an insulating state at $\nu = -1$ filling with a non-zero displacement field in region III. Such a phase does not occur at $\nu = -3$ or $\nu = -2$ fillings.

Region IV: the displacement field is further increased (e.g., $U \gtrsim 220\,\text{meV}$ at $w_0/w_1 = 0.2$). Similar to the strong field phase at $\nu = -3$ and $\nu = -2$, the increased bandwidth of the non-interacting dispersion becomes comparable to or larger than the strength of the Coulomb interaction. Therefore, the electrons will first occupy the low energy states around K_M and K'_M at $E - E_F \approx -90\,\text{meV}$ which can be seen in Fig. 6(d). A large Fermi surface can also be observed in the band structure, which implies that region IV is a metallic phase. Both the valley polarization N_v/N_M and the intervalley coherence $\mathcal{C}$ are nearly zero in this region.

In summary, there are four phases in the phase diagram at filling factor $\nu = -1$. When the displacement field is close to zero, i.e., in region I, the ground state is an intervalley coherent semimetal. As the displacement field increases into region II, the ground state becomes a semimetal without intervalley coherence. When the field further increases into region III, the HF band structure becomes gapped, and therefore the ground state is an insulator. We note that this phase does not occur at fillings $\nu = -3$ and $\nu = -2$. Finally in region IV with the strongest displacement field, the system becomes a metal, similar to the filling factors $\nu = -3$ and $\nu = -2$.

VII. NUMERICAL RESULTS AT FILLING FACTOR $\nu = 0$

Lastly, we present our HF calculation results for TSTG at filling factor $\nu = 0$. In comparison, in the TBG system the ground state at $\nu = 0$ is an insulator state with four occupied intervalley coherent bands and zero total Chern number [70, 107]. Similar to other integer fillings, we expect the ground state of TSTG at $\nu = 0$ and $U = 0$ to be the tensor product of a TBG intervalley coherent insulator ground state and half filled Dirac semimetal.

In Fig. 7(a), we show the intervalley coherence $\mathcal{C}$ in the w_0/w_1 and U parameter space at $\nu = 0$. By using the same method as the HF band structure along the high symmetry lines, which is discussed in Appendix B 2, we can estimate the HF Hamiltonian $\mathcal{H}^{HF}(\mathbf{k})$ at any momenta not included in the momentum lattice employed in our HF iterations. Thus, the energy gap around the Fermi level along the high symmetry lines as a function of w_0/w_1 and U can be calculated, which is shown in Fig. 7(b). We are able to identify three different regions I, II and III in the w_0/w_1 and U parameter space, based on the valley coherence $\mathcal{C}$ and the energy gap. Other HF quantities at fixed $w_0/w_1 = 0.2$ and $w_0/w_1 = 0.8$ are also

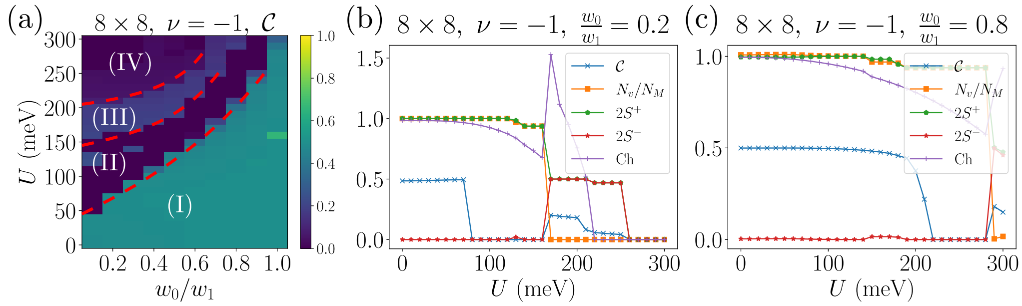

FIG. 5. (a) The phase diagram at filling factor $\nu = -1$ obtained on a 8×8 momentum lattice in the (w_0, U) parameter space. The color represents the intervalley coherence $\mathcal{C}$. (b) and (c) The displacement field dependence of physical quantities $\mathcal{C}, N_v, \mathrm{Ch}$ and $S^{\pm}$ on 8×8 at fixed $w_0/w_1 = 0.2$ (b) and $w_0/w_1 = 0.8$ (c).

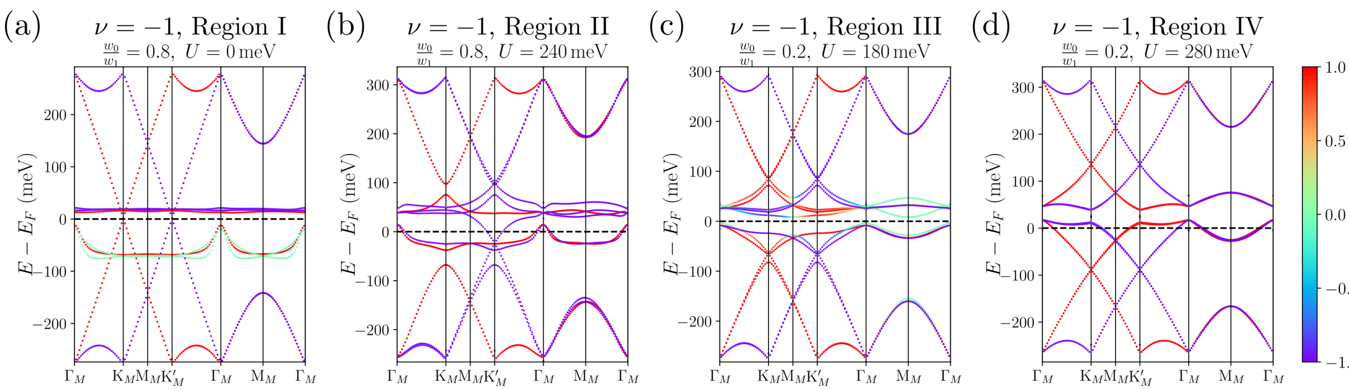

FIG. 6. The HF band structure at $w_0/w_1 = 0.8$ for $U = 0$ in region I (a), $w_0/w_1 = 0.8$ for $U = 240\,\mathrm{meV}$ in region II (b), $w_0/w_1 = 0.2$ for $U = 180\,\mathrm{meV}$ in region III (c) and $w_0/w_1 = 0.2$ for $U = 280\,\mathrm{meV}$ in region IV (d) on a 10×10 lattice at filling factor $\nu = -1$. The color represents the valley polarization $v_i(\mathbf{k})$ of each single body state.

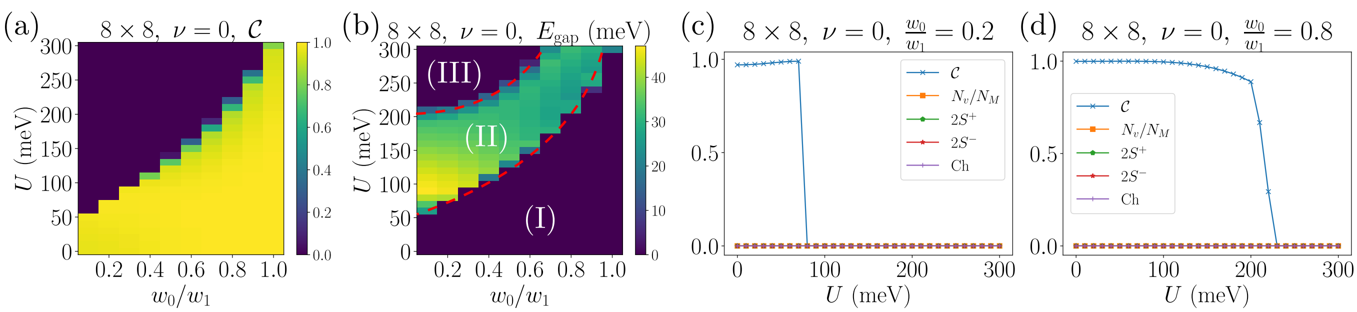

FIG. 7. Phase diagrams at filling factor $\nu = 0$. (a) The two dimensional phase diagram on 8×8 momentum lattice in (w_0, U) parameter space. It can be seen that in the weak U phase, the intervalley coherence $\mathcal{C} \approx 1$ shows that there are four occupied intervalley coherent bands. (b) The energy gap along the high symmetry lines as a function of w_0/w_1 and U. Here we use the method discussed in Appendix B 2 to obtain the Hartree-Fock Hamiltonian along the high symmetry lines, therefore we are able to estimate the energy gap from the 8×8 lattice. (c) and (d) The displacement field dependence of several quantities $\mathcal{C}, N_v, S^{\pm}$ and Ch on 8×8 lattice with $w_0/w_1 = 0.2$ (c) and $w_0/w_1 = 0.8$ (d).

shown in Figs. 7(c) and (d). We now use these quantities to describe the HF ground states in these regions.

Region I: this region is in the low displacement field regime, and we find the values of the HF quantities are $\mathcal{C} \approx 1$, $N_v/N_M \approx 0$, $\mathrm{Ch} \approx 0$ and $S^{\pm} \approx 0$. The value of the intervalley coherence $\mathcal{C} \approx 1$ shows that there are four occupied intervalley coherent bands and have zero total Chern number. Therefore, these values indicates that the HF ground state at $U = 0$ can be well approximated by the tensor product of the insulating intervalley coherent TBG ground state at $\nu_{\mathrm{TBG}} = 0$ predicted in Refs. [70, 107], and the ground state at $U > 0$ in region I is adiabatically connected to this tensor product state. A typical HF band structure can be found in Fig. 8(a).

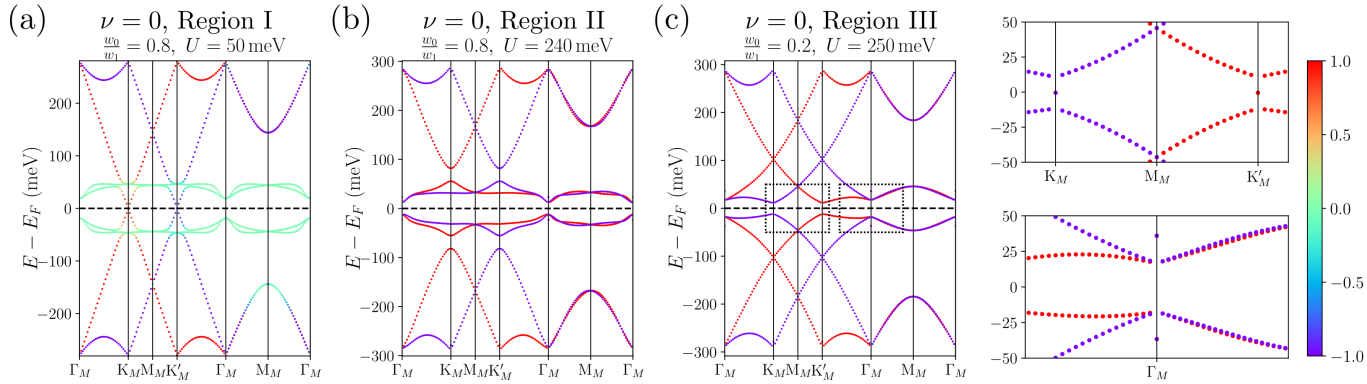

FIG. 8. (a-c) The HF band structure on a 10×10 lattice at filling factor $\nu = 0$ at $w_0/w_1 = 0.8$ for $U = 50\,\mathrm{meV}$ in region I (a), at $w_0/w_1 = 0.8$ for $U = 200\,\mathrm{meV}$ in region II (b) and at $w_0/w_1 = 0.2$ for $U = 250\,\mathrm{meV}$ in region III (c), respectively. The color stands for the valley polarization $v_i(\mathbf{k})$ of each single body state. The zoom in band structures around K_M, K'_M and Γ_M points in the dashed boxes in subfigure (c) are also shown. It is visible that the HF band structure is discontinuous at these points, and it is also gapless at K_M and K'_M points.

The occupied flat bands have zero valley polarization, which agree with the intervalley coherent ground state. Therefore, the $\nu = 0$ TSTG ground state is an intervalley coherent semimetal. As we show in Appendix D, the gapless Dirac nodes of this phase at $U > 0$ is protected by a remaining anti-unitary symmetry $\mathcal{G}_\gamma$ ($\mathcal{G}_\gamma^2 = 1$), which is a combination of the $C_{2z}T$ and a relative phase rotation between the two valleys.

Region II: the displacement field is intermediate, and as seen in both Figs. 7(b) and (c), the intervalley coherence $\mathcal{C}$ drops to zero in this region. Other HF parameters, including N_v/N_M, Ch and $S^{\pm}$ are equal to zero in region II. We also notice that there is another state with non-zero Ch values in region II, whose energy increment from the state with Ch $= 0$ is within the machine precision when the parameters are around the boundary between regions II and III, showing a possible competing order. A typical HF ground state band structure in region II is shown in Fig. 8(b). The occupied flat bands have valley polarization values $v_i(\mathbf{k}) \approx \pm 1$, and there is a large direct gap around the Fermi level. This result indicates that region II is an insulating phase, akin to the region III at $\nu = -1$ filling.

Region III: here the interlayer potential U is stronger, and the HF quantities $\mathcal{C}$, N_v/N_M, Ch and $S^{\pm}$ in this large U region are the same as in region II. However, the band structures undergo an abrupt transition. As discussed in previous sections, the bandwidth of the low energy bands become large when U is large, and therefore the effect of the interaction will be suppressed by the kinetic energy. A HF band structure in this region is shown in Fig. 8(c). The HF mean field band structure is similar to the non-interacting band dispersion, which has gapless Dirac points at K_M and K'_M points. The discontinuous dispersions in Fig. 8(c) at K_M and K'_M (see the zoom-in plots in Fig. 8(c)) are due to neglecting of the higher bands in the TSTG projected Hamiltonian, as explained in Appendix A. From the HF band structure, we conclude that the large displacement field phase in region III at filling $\nu = 0$ becomes a semimetal.

To summarize, there are three phases at filling factor $\nu = 0$, as shown in Fig. 7(b). Within the small U region I, the HF ground state is an intervalley coherent semimetal. In region II with an intermediate U, the ground state is an insulator without intervalley coherence or valley polarization. Finally, in region III with a large U, the system becomes a semimetal with no valley polarization or intervalley coherence.

VIII. CONCLUSION

Through projected Hartree-Fock mean field calculations, our work unveiled the close relationship between TSTG at weak displacement field and TBG systems at integer fillings $\nu = -3, -2, -1$ and 0. We show that at weak displacement fields, the TSTG ground states at integer fillings are almost semimetal states which are in the same phase as the tensor product of the TBG ground states at the same filling and a Dirac semimetal. Beyond the phases inherited from the TBG physics, the TSTG undergoes transitions into large Fermi surface metals or insulators as the displacement field increases. Besides, we generically find that the displacement field destabilizes the intervalley coherence of the flat bands.

For filling factor $\nu = -3$, we found three regions of different phases. At small displacement field, the TSTG ground state is a semimetal with an occupied spin-valley polarized flat band when $w_0/w_1 \lesssim 0.6$. At large displacement fields, the TSTG undergoes a first order phase transition into a metallic phase with large Fermi surfaces and zero valley polarization, due to the enlarged band width. When $w_0/w_1 \gtrsim 0.7$ and $U = 0$, we observed that the electrons transfer from the Dirac cones into the TBG flat bands, which yields a metallic phase with competing orders. Moreover, similar to pure TBG systems at $\nu = -3$, it is possible to have translation symmetry breaking, some evidence of which is shown in Appendix C 1. We leave the study of translation breaking TSTG phases in the future.

For filling factors $\nu = -2, -1$ and 0, our HF numerical results show that the TSTG ground states at weak displacement fields are semimetals with intervalley coherent flat bands occupied. At intermediate displacement fields, the intervalley coherence drops abruptly to zero, signaling a transition into phases without intervalley coherence, which are either semimetals (at $\nu = -2$ and -1) or insulators (at $\nu = -1$ and $\nu = 0$). With a stronger displacement field, the dispersive energy bands will have bandwidths exceeding the energy scale of Coulomb interactions, which leads the system into a metallic state with little valley polarization or intervalley coherence.

Our work reveals two roles of the displacement field in TSTG with Coulomb interaction: destabilizing the intervalley coherence (if any), and increasing the flat band width and thus weakening the correlations due to interactions. Our results may provide guidance to the analytical studies of TSTG ground states in the future.

ACKNOWLEDGMENTS

We are grateful to Zhi-Da Song for previous collaboration on related works and enlightening discussions. We thank Oskar Vafek, Pablo Jarillo-Herrero, and Dmitri Efetov for fruitful discussions. This work was supported primarily by the ONR No. N00014-20-1-2303, the Schmidt Fund for Innovative Research, Simons Investigator Grant No. 404513, the Packard Foundation, the Gordon and Betty Moore Foundation through Grant No. GBMF8685 towards the Princeton theory program, and a Guggenheim Fellowship from the John Simon Guggenheim Memorial Foundation. Further support was provided by the NSF-EAGER No. DMR 1643312, NSF-MRSEC No. DMR-1420541 and DMR-2011750, DOE Grant No. DE-SC0016239 , Gordon and Betty Moore Foundation through Grant GBMF8685 towards the Princeton theory program, BSF Israel US foundation No. 2018226, and the Princeton Global Network Funds. B.L. acknowledges support from the Alfred P. Sloan Foundation.

Note added.—During the final preparation of this manuscript, a recent preprint Ref. [130] appeared, with numerical results consistent with ours at even integer fillings.

[1] J. M. B. Lopes dos Santos, N. M. R. Peres, and A. H. Castro Neto, Phys. Rev. Lett. **99**, 256802 (2007).

[2] E. Suárez Morell, J. D. Correa, P. Vargas, M. Pacheco, and Z. Barticevic, Phys. Rev. B **82**, 121407 (2010).

[3] R. Bistritzer and A. H. MacDonald, PNAS **108**, 12233 (2011).

[4] Y. Cao, V. Fatemi, A. Demir, S. Fang, S. L. Tomarken, J. Y. Luo, J. D. Sanchez-Yamagishi, K. Watanabe, T. Taniguchi, E. Kaxiras, R. C. Ashoori, and P. Jarillo-Herrero, Nature **556**, 80 (2018).

[5] Y. Cao, V. Fatemi, S. Fang, K. Watanabe, T. Taniguchi, E. Kaxiras, and P. Jarillo-Herrero, Nature **556**, 43 (2018).

[6] Y. Cao, D. Chowdhury, D. Rodan-Legrain, O. Rubies-Bigorda, K. Watanabe, T. Taniguchi, T. Senthil, and P. Jarillo-Herrero, Phys. Rev. Lett. **124**, 076801 (2020).

[7] G. Chen, A. L. Sharpe, E. J. Fox, Y.-H. Zhang, S. Wang, L. Jiang, B. Lyu, H. Li, K. Watanabe, T. Taniguchi, Z. Shi, T. Senthil, D. Goldhaber-Gordon, Y. Zhang, and F. Wang, Nature **579**, 56 (2020).

[8] X. Liu, Z. Wang, K. Watanabe, T. Taniguchi, O. Vafek, and J. I. A. Li, Science **371**, 1261 (2021), https://science.sciencemag.org/content/371/6535/1261.full.pdf.

[9] X. Lu, P. Stepanov, W. Yang, M. Xie, M. A. Aamir, I. Das, C. Urgell, K. Watanabe, T. Taniguchi, G. Zhang, A. Bachtold, A. H. MacDonald, and D. K. Efetov, Nature **574**, 653 (2019).

[10] X. Lu, B. Lian, G. Chaudhary, B. A. Piot, G. Romagnoli, K. Watanabe, T. Taniguchi, M. Poggio, A. H. MacDonald, B. A. Bernevig, and D. K. Efetov, arXiv:2006.13963 [cond-mat] (2020), arXiv:2006.13963 [cond-mat].

[11] J. M. Park, Y. Cao, K. Watanabe, T. Taniguchi, and P. Jarillo-Herrero, Nature **592**, 43 (2021).

[12] H. Polshyn, M. Yankowitz, S. Chen, Y. Zhang, K. Watanabe, T. Taniguchi, C. R. Dean, and A. F. Young, Nat. Phys. **15**, 1011 (2019).

[13] Y. Saito, J. Ge, K. Watanabe, T. Taniguchi, and A. F. Young, Nat. Phys. **16**, 926 (2020).

[14] Y. Saito, J. Ge, L. Rademaker, K. Watanabe, T. Taniguchi, D. A. Abanin, and A. F. Young, Nat. Phys. , 1 (2021).

[15] M. Serlin, C. L. Tschirhart, H. Polshyn, Y. Zhang, J. Zhu, K. Watanabe, T. Taniguchi, L. Balents, and A. F. Young, Science **367**, 900 (2020).

[16] P. Stepanov, I. Das, X. Lu, A. Fahimniya, K. Watanabe, T. Taniguchi, F. H. L. Koppens, J. Lischner, L. Levitov, and D. K. Efetov, Nature **583**, 375 (2020).

[17] S. Wu, Z. Zhang, K. Watanabe, T. Taniguchi, and E. Y. Andrei, Nature Materials **20**, 488 (2021).

[18] M. Yankowitz, S. Chen, H. Polshyn, Y. Zhang, K. Watanabe, T. Taniguchi, D. Graf, A. F. Young, and C. R. Dean, Science **363**, 1059 (2019).

[19] Y. Choi, J. Kemmer, Y. Peng, A. Thomson, H. Arora, R. Polski, Y. Zhang, H. Ren, J. Alicea, G. Refael, F. von Oppen, K. Watanabe, T. Taniguchi, and S. Nadj-Perge, Nat. Phys. **15**, 1174 (2019).

[20] Y. Choi, H. Kim, Y. Peng, A. Thomson, C. Lewandowski, R. Polski, Y. Zhang, H. S. Arora, K. Watanabe, T. Taniguchi, J. Alicea, and S. Nadj-Perge, arXiv:2008.11746 [cond-mat] (2020), arXiv:2008.11746 [cond-mat].

[21] A. Kerelsky, L. J. McGilly, D. M. Kennes, L. Xian, M. Yankowitz, S. Chen, K. Watanabe, T. Taniguchi,

J. Hone, C. Dean, A. Rubio, and A. N. Pasupathy, Nature **572**, 95 (2019).
[22] K. P. Nuckolls, M. Oh, D. Wong, B. Lian, K. Watanabe, T. Taniguchi, B. A. Bernevig, and A. Yazdani, Nature **588**, 610 (2020).
[23] D. Wong, K. P. Nuckolls, M. Oh, B. Lian, Y. Xie, S. Jeon, K. Watanabe, T. Taniguchi, B. A. Bernevig, and A. Yazdani, Nature **582**, 198 (2020).
[24] Y. Xie, B. Lian, B. Jäck, X. Liu, C.-L. Chiu, K. Watanabe, T. Taniguchi, B. A. Bernevig, and A. Yazdani, Nature **572**, 101 (2019).
[25] Y. Jiang, X. Lai, K. Watanabe, T. Taniguchi, K. Haule, J. Mao, and E. Y. Andrei, Nature **573**, 91 (2019).
[26] Y. Choi, H. Kim, C. Lewandowski, Y. Peng, A. Thomson, R. Polski, Y. Zhang, K. Watanabe, T. Taniguchi, J. Alicea, and S. Nadj-Perge, arXiv:2102.02209 [cond-mat] (2021), arXiv:2102.02209 [cond-mat].
[27] J. Kang and O. Vafek, Phys. Rev. Lett. **122**, 246401 (2019).
[28] K. Seo, V. N. Kotov, and B. Uchoa, Phys. Rev. Lett. **122**, 246402 (2019).
[29] N. Bultinck, E. Khalaf, S. Liu, S. Chatterjee, A. Vishwanath, and M. P. Zaletel, Phys. Rev. X **10**, 031034 (2020).
[30] K. Hejazi, X. Chen, and L. Balents, Phys. Rev. Research **3**, 013242 (2021).
[31] R. M. Fernandes and L. Fu, arXiv:2101.07943 [cond-mat] (2021), arXiv:2101.07943 [cond-mat].
[32] R. M. Fernandes and J. W. F. Venderbos, Science Advances **6**, eaba8834 (2020).
[33] J. W. F. Venderbos and R. M. Fernandes, Phys. Rev. B **98**, 245103 (2018).
[34] P. Potasz, M. Xie, and A. H. MacDonald, arXiv:2102.02256 [cond-mat] (2021), arXiv:2102.02256 [cond-mat].
[35] A. Abouelkomsan, Z. Liu, and E. J. Bergholtz, Phys. Rev. Lett. **124**, 106803 (2020).
[36] J. Ahn, S. Park, and B.-J. Yang, Phys. Rev. X **9**, 021013 (2019).
[37] B. A. Bernevig, Z.-D. Song, N. Regnault, and B. Lian, Phys. Rev. B **103**, 205411 (2021).
[38] B. A. Bernevig, Z.-D. Song, N. Regnault, and B. Lian, Phys. Rev. B **103**, 205413 (2021).
[39] B. A. Bernevig, B. Lian, A. Cowsik, F. Xie, N. Regnault, and Z.-D. Song, Phys. Rev. B **103**, 205415 (2021).
[40] N. Bultinck, S. Chatterjee, and M. P. Zaletel, Phys. Rev. Lett. **124**, 166601 (2020).
[41] J. Cao, M. Wang, C.-C. Liu, and Y. Yao, arXiv:2012.02575 [cond-mat] (2020), arXiv:2012.02575 [cond-mat].
[42] T. Cea and F. Guinea, Phys. Rev. B **102**, 045107 (2020).
[43] M. Christos, S. Sachdev, and M. S. Scheurer, PNAS **117**, 29543 (2020).
[44] L. Classen, C. Honerkamp, and M. M. Scherer, Phys. Rev. B **99**, 195120 (2019).
[45] Y. Da Liao, Z. Y. Meng, and X. Y. Xu, Phys. Rev. Lett. **123**, 157601 (2019).
[46] Y. Da Liao, J. Kang, C. N. Breiø, X. Y. Xu, H.-Q. Wu, B. M. Andersen, R. M. Fernandes, and Z. Y. Meng, Phys. Rev. X **11**, 011014 (2021).
[47] S. Dai, Y. Xiang, and D. J. Srolovitz, Nano Lett. **16**, 5923 (2016).
[48] J. F. Dodaro, S. A. Kivelson, Y. Schattner, X. Q. Sun, and C. Wang, Phys. Rev. B **98**, 075154 (2018).
[49] D. K. Efimkin and A. H. MacDonald, Phys. Rev. B **98**, 035404 (2018).
[50] P. Eugenio and C. Dag, SciPost Physics Core **3**, 015 (2020).
[51] J. González and T. Stauber, Phys. Rev. Lett. **122**, 026801 (2019).
[52] F. Guinea and N. R. Walet, PNAS **115**, 13174 (2018).
[53] H. Guo, X. Zhu, S. Feng, and R. T. Scalettar, Phys. Rev. B **97**, 235453 (2018).
[54] K. Hejazi, C. Liu, H. Shapourian, X. Chen, and L. Balents, Phys. Rev. B **99**, 035111 (2019).
[55] K. Hejazi, C. Liu, and L. Balents, Phys. Rev. B **100**, 035115 (2019).
[56] T. Huang, L. Zhang, and T. Ma, Science Bulletin **64**, 310 (2019).
[57] Y. Huang, P. Hosur, and H. K. Pal, Phys. Rev. B **102**, 155429 (2020).
[58] H. Isobe, N. F. Q. Yuan, and L. Fu, Phys. Rev. X **8**, 041041 (2018).
[59] S. K. Jain, V. Juričić, and G. T. Barkema, 2D Mater. **4**, 015018 (2016).
[60] A. Julku, T. J. Peltonen, L. Liang, T. T. Heikkilä, and P. Törmä, Phys. Rev. B **101**, 060505 (2020).
[61] J. Kang and O. Vafek, Phys. Rev. X **8**, 031088 (2018).
[62] J. Kang and O. Vafek, Phys. Rev. B **102**, 035161 (2020).
[63] D. M. Kennes, J. Lischner, and C. Karrasch, Phys. Rev. B **98**, 241407 (2018).
[64] E. Khalaf, S. Chatterjee, N. Bultinck, M. P. Zaletel, and A. Vishwanath, Science Advances **7**, 10.1126/sciadv.abf5299 (2021), https://advances.sciencemag.org/content/7/19/eabf5299.full.pdf.
[65] E. J. König, P. Coleman, and A. M. Tsvelik, Phys. Rev. B **102**, 104514 (2020).
[66] M. Koshino, N. F. Q. Yuan, T. Koretsune, M. Ochi, K. Kuroki, and L. Fu, Phys. Rev. X **8**, 031087 (2018).
[67] P. J. Ledwith, G. Tarnopolsky, E. Khalaf, and A. Vishwanath, Phys. Rev. Research **2**, 023237 (2020).
[68] C. Lewandowski, D. Chowdhury, and J. Ruhman, Phys. Rev. B **103**, 235401 (2021).
[69] B. Lian, Z. Wang, and B. A. Bernevig, Phys. Rev. Lett. **122**, 257002 (2019).
[70] B. Lian, Z.-D. Song, N. Regnault, D. K. Efetov, A. Yazdani, and B. A. Bernevig, Phys. Rev. B **103**, 205414 (2021).
[71] B. Lian, F. Xie, and B. A. Bernevig, Phys. Rev. B **102**, 041402 (2020).
[72] Z. Liu, E. J. Bergholtz, H. Fan, and A. M. Läuchli, Phys. Rev. Lett. **109**, 186805 (2012).
[73] C.-C. Liu, L.-D. Zhang, W.-Q. Chen, and F. Yang, Phys. Rev. Lett. **121**, 217001 (2018).
[74] J. Liu, J. Liu, and X. Dai, Phys. Rev. B **99**, 155415 (2019).
[75] J. Liu and X. Dai, Phys. Rev. B **103**, 035427 (2021).
[76] S. Liu, E. Khalaf, J. Y. Lee, and A. Vishwanath, Phys. Rev. Research **3**, 013033 (2021).
[77] M. Ochi, M. Koshino, and K. Kuroki, Phys. Rev. B **98**, 081102 (2018).
[78] B. Padhi, A. Tiwari, T. Neupert, and S. Ryu, Phys. Rev. Research **2**, 033458 (2020).
[79] T. J. Peltonen, R. Ojajärvi, and T. T. Heikkilä, Phys. Rev. B **98**, 220504 (2018).
[80] H. C. Po, L. Zou, A. Vishwanath, and T. Senthil, Phys. Rev. X **8**, 031089 (2018).
[81] H. C. Po, L. Zou, T. Senthil, and A. Vishwanath, Phys.

Rev. B **99**, 195455 (2019).
[82] C. Repellin, Z. Dong, Y.-H. Zhang, and T. Senthil, Phys. Rev. Lett. **124**, 187601 (2020).
[83] C. Repellin and T. Senthil, Phys. Rev. Research **2**, 023238 (2020).
[84] B. Roy and V. Juričić, Phys. Rev. B **99**, 121407 (2019).
[85] T. Soejima, D. E. Parker, N. Bultinck, J. Hauschild, and M. P. Zaletel, Phys. Rev. B **102**, 205111 (2020).
[86] Z. Song, Z. Wang, W. Shi, G. Li, C. Fang, and B. A. Bernevig, Phys. Rev. Lett. **123**, 036401 (2019).
[87] Z.-D. Song, B. Lian, N. Regnault, and B. A. Bernevig, Phys. Rev. B **103**, 205412 (2021).
[88] G. Tarnopolsky, A. J. Kruchkov, and A. Vishwanath, Phys. Rev. Lett. **122**, 106405 (2019).
[89] A. Thomson, S. Chatterjee, S. Sachdev, and M. S. Scheurer, Phys. Rev. B **98**, 075109 (2018).
[90] K. Uchida, S. Furuya, J.-I. Iwata, and A. Oshiyama, Phys. Rev. B **90**, 155451 (2014).
[91] O. Vafek and J. Kang, Phys. Rev. Lett. **125**, 257602 (2020).
[92] J. Wang, Y. Zheng, A. J. Millis, and J. Cano, Phys. Rev. Research **3**, 023155 (2021).
[93] M. M. van Wijk, A. Schuring, M. I. Katsnelson, and A. Fasolino, 2D Mater. **2**, 034010 (2015).
[94] J. H. Wilson, Y. Fu, S. Das Sarma, and J. H. Pixley, Phys. Rev. Research **2**, 023325 (2020).
[95] F. Wu, A. H. MacDonald, and I. Martin, Phys. Rev. Lett. **121**, 257001 (2018).
[96] X.-C. Wu, C.-M. Jian, and C. Xu, Phys. Rev. B **99**, 161405 (2019).
[97] F. Wu, E. Hwang, and S. Das Sarma, Phys. Rev. B **99**, 165112 (2019).
[98] F. Wu and S. Das Sarma, Phys. Rev. Lett. **124**, 046403 (2020).
[99] F. Xie, Z. Song, B. Lian, and B. A. Bernevig, Phys. Rev. Lett. **124**, 167002 (2020).
[100] F. Xie, A. Cowsik, Z.-D. Song, B. Lian, B. A. Bernevig, and N. Regnault, Phys. Rev. B **103**, 205416 (2021).
[101] M. Xie and A. H. MacDonald, Phys. Rev. Lett. **124**, 097601 (2020).
[102] M. Xie and A. H. MacDonald, arXiv:2010.07928 [cond-mat] (2020), arXiv:2010.07928 [cond-mat].
[103] C. Xu and L. Balents, Phys. Rev. Lett. **121**, 087001 (2018).
[104] X. Y. Xu, K. T. Law, and P. A. Lee, Phys. Rev. B **98**, 121406 (2018).
[105] Y.-Z. You and A. Vishwanath, npj Quantum Mater. **4**, 1 (2019).
[106] N. F. Q. Yuan and L. Fu, Phys. Rev. B **98**, 045103 (2018).
[107] Y. Zhang, K. Jiang, Z. Wang, and F. Zhang, Phys. Rev. B **102**, 035136 (2020).
[108] L. Zou, H. C. Po, A. Vishwanath, and T. Senthil, Phys. Rev. B **98**, 085435 (2018).
[109] Y. H. Kwan, G. Wagner, T. Soejima, M. P. Zaletel, S. H. Simon, S. A. Parameswaran, and N. Bultinck, arXiv e-prints , arXiv:2105.05857 (2021), arXiv:2105.05857 [cond-mat.str-el].
[110] X. Zhang, G. Pan, Y. Zhang, J. Kang, and Z. Y. Meng, Chinese Physics Letters **38**, 077305 (2021).
[111] E. Suárez Morell, M. Pacheco, L. Chico, and L. Brey, Phys. Rev. B **87**, 125414 (2013).
[112] E. Khalaf, A. J. Kruchkov, G. Tarnopolsky, and A. Vishwanath, Phys. Rev. B **100**, 085109 (2019).
[113] C. Mora, N. Regnault, and B. A. Bernevig, Phys. Rev. Lett. **123**, 026402 (2019).
[114] X. Li, F. Wu, and A. H. MacDonald, arXiv:1907.12338 [cond-mat] (2019), arXiv:1907.12338 [cond-mat].
[115] A. Lopez-Bezanilla and J. L. Lado, Phys. Rev. Research **2**, 033357 (2020).
[116] S. Carr, C. Li, Z. Zhu, E. Kaxiras, S. Sachdev, and A. Kruchkov, Nano Lett. **20**, 3030 (2020).
[117] Y. Park, B. L. Chittari, and J. Jung, Phys. Rev. B **102**, 035411 (2020).
[118] Z. Zhu, S. Carr, D. Massatt, M. Luskin, and E. Kaxiras, Phys. Rev. Lett. **125**, 116404 (2020).
[119] C. Lei, L. Linhart, W. Qin, F. Libisch, and A. H. MacDonald, arXiv:2010.05787 [cond-mat] (2020), arXiv:2010.05787 [cond-mat].
[120] Z. Wu, Z. Zhan, and S. Yuan, Science China Physics, Mechanics & Astronomy **64**, 1 (2021).
[121] Z. Hao, A. M. Zimmerman, P. Ledwith, E. Khalaf, D. H. Najafabadi, K. Watanabe, T. Taniguchi, A. Vishwanath, and P. Kim, Science **371**, 1133 (2021), https://science.sciencemag.org/content/371/6534/1133.full.pdf.
[122] J. M. Park, Y. Cao, K. Watanabe, T. Taniguchi, and P. Jarillo-Herrero, Nature **590**, 249 (2021).
[123] Y. Cao, J. M. Park, K. Watanabe, T. Taniguchi, and P. Jarillo-Herrero, arXiv e-prints , arXiv:2103.12083 (2021), arXiv:2103.12083 [cond-mat.mes-hall].
[124] D. Călugăru, F. Xie, Z.-D. Song, B. Lian, N. Regnault, and B. A. Bernevig, Phys. Rev. B **103**, 195411 (2021).
[125] J. Shin, B. Lingam Chittari, and J. Jung, arXiv e-prints , arXiv:2104.01570 (2021), arXiv:2104.01570 [cond-mat.mes-hall].
[126] A. Fischer, Z. A. H. Goodwin, A. A. Mostofi, J. Lischner, D. M. Kennes, and L. Klebl, arXiv e-prints , arXiv:2104.10176 (2021), arXiv:2104.10176 [cond-mat.supr-con].
[127] E. Lake and T. Senthil, arXiv e-prints , arXiv:2104.13920 (2021), arXiv:2104.13920 [cond-mat.supr-con].
[128] W. Qin and A. H. MacDonald, arXiv e-prints , arXiv:2104.14026 (2021), arXiv:2104.14026 [cond-mat.mes-hall].
[129] Y.-Z. Chou, F. Wu, J. D. Sau, and S. Das Sarma, arXiv e-prints , arXiv:2105.00561 (2021), arXiv:2105.00561 [cond-mat.supr-con].
[130] M. Christos, S. Sachdev, and M. S. Scheurer, arXiv e-prints , arXiv:2106.02063 (2021), arXiv:2106.02063 [cond-mat.str-el].